Chapter 4: Molecular Nonporous compounds for adsorption-desorption

Accommodative 'Molecular' Behavior of Non-porous Crystal at Solid-Gas and Solid-Liquid Interfaces

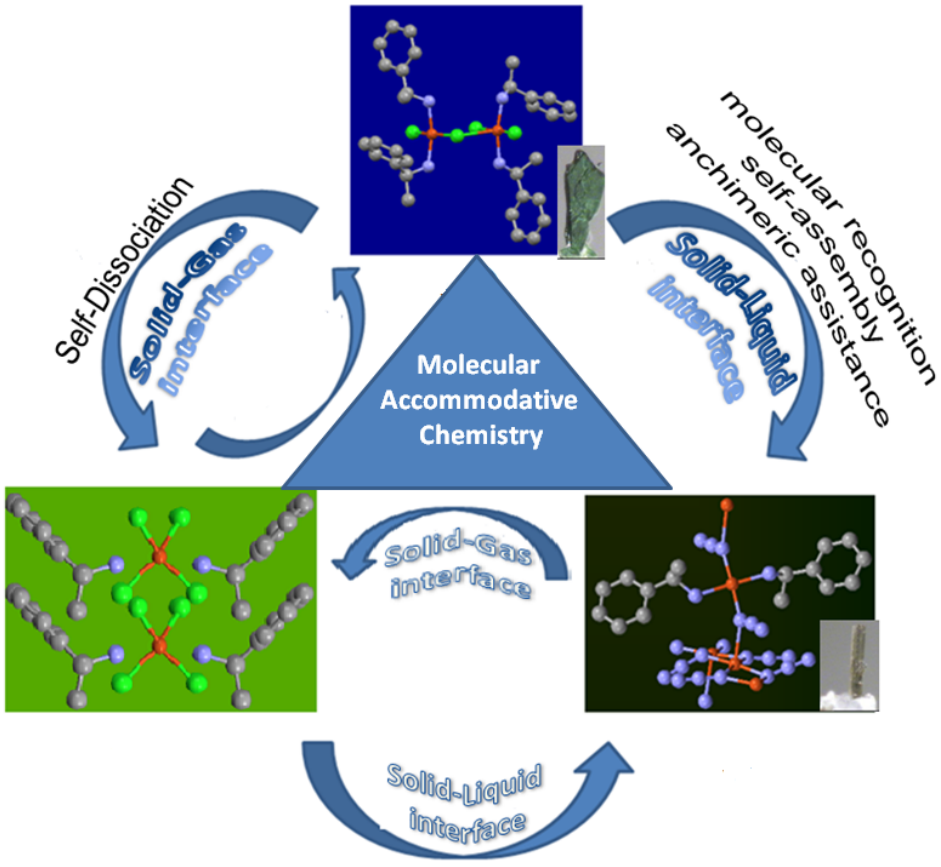

Introduction

Designing of 'unique' smart material capable of operating at maximum possible interfaces to display swift and prominent change of a 'measurable property' due to change in external chemical or physical stimuli has been of keen interest in science. The field has been of profound importance in technology, environmental safety and energy issues for which ideal target materials are based on molecular compounds. Molecular compounds are not only flexible but are easily 'responsive' for various weak non-covalent interactions in their vicinity. This property of molecular compounds has driven research in coordination polymers or metal-organic framework (MOF) compounds to form porous "containers" for host compounds, particularly in last two decades.[1, 2] Typically, these types of compounds act as 'sensor' materials by efficiently adsorbing-desorbing various guest molecules in their porous void spaces due to non-covalent interactions. Ideally a sensor compound during sorption-desorption must show (a) change in colour (optical property); (b) change in structural symmetry (polar space group to non-polar space group or *vice-versa*); (c) selectivity for specific guest molecules; (d) complete reversibility of sorption/desorption; and (e) retention of crystalline or solid-state character.

Most of these sensors work at solid-gas interfaces by adsorption-desorption of gases, and at solid-liquid interfaces by molecular recognition based incorporation of ions. But to date, to our best knowledge, no sensor has shown ability to work at both solid-gas and solid-liquid interfaces. This may be due to a complete difference in structural designing principles and mechanism of interaction involved at these interfaces. The major dissimilarity with respect to structural design remains in the geometry of the central metal ion and the type of organic ligands employed. For solid-gas interfaces, mixed square planar and octahedral geometry of the metal ion is preferred with carboxylic acids or secondary amines as organic ligands for generating rigid extended porous[1] or non-porous structures[3,4]. This is in contrast to flexible networks of mainly with mixed tetrahedral and octahedral structures with metal-ether, or metal-primary amine linkages used for solid-liquid interfacial molecular recognition purpose[2]. We mixed these two structural designing aspects, by employingisolated central metal centers with primary amines as ligands, to form a unique chemical sensor which operates at solid-gas and

solid-liquid interface. This material offers both rigidity and structural reversibility due to its square planar structure withmolecular recognition dynamism due to the primary amines.We observed this helped molecular crystal to 'extend' its purely molecular property or to express its 'molecular' behaviour in the form of 'good host' to welcome guest molecules from gas phase as well as liquid phase. This also helped in revealing chemistry behind the crystal to crystal transformation observed during our present work. To our best knowledge, square planar-primary amine based Cu(II) structures are very rare. Concurrently, we [5] synthesized a series of structurally similar non-porous materials, by the reaction of aniline and benzylaminederivatives with $CuCl_2$. Finally, we show the reversible in-take of (1) HCl gas at solid-gas interfaces, and (2) selectively "accommodative" or self-assembled N_3^- anion at solid-liquid interfaces for the whole family of materials with crystal to crystal transformation, representatively shown for one compound in Figure 4.1.

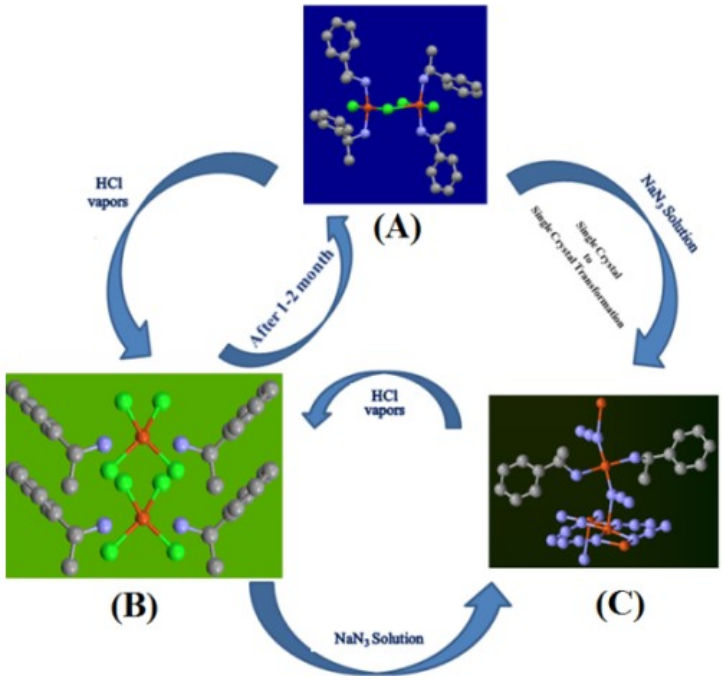

Fig. 4.1: Molecular Accommodative Chemistry with visual colour change: Non-porous Cu(II) complex, $(C_6H_5CH(CH_3)NH_2)_2CuCl_2$ (A) when exposed to HCl gas (solid-gas reaction) reversibly changes to $(C_6H_5CH(CH_3)NH_3)_2CuCl_4$, double salt (B). (A) at solid-liquid interface shows Single-Crystal to Single Crystal transformation by selectively absorbing azide anion driven macromolecular assembly to form $[Cu_3(C_6H_5CH(CH_3)NH_3)_2(N_3)_6]_n$(C). (B) transforms reversibly to (C)

In literature similar in-take of HCl gas at solid-gas interface by non-porous molecular crystals have been considered as sorption-desorption. This is partially correct, as HCl gas is taken-in and given-out in the reversible process. But in an ideal adsorption process, HCl gas should not 'self-dissociate' into H^+ cation and Cl^- anion, which is a case here and in literature. This makes us to consider it as an 'accomodative' process. We term 'accomomdative' behavior for 'breathing' nature of inner and outer coordination sphere around metal ion which imposes change in coordination geometry and is driven by self-dissociation, self-assembly, molecular recognition, and/or anchimeric assistance in solid state, akin to an archetypal molecular property in liquid state.

Abstract: Interaction of Molecular crystals with guest molecules at solid-gas and solid-liquid interface differs because of characteristically dissimilar structural frameworks acting as host molecules at these interfaces. This limits on designing of uniquely structured molecular compounds which can work at both these interfaces. In pursuit of our studies, we observed a non-porous molecular solid crystal, dinuclear copper complex $(C_6H_5CH(X)NH_2)_2CuCl_2$, to reversibly chemisorbs HCl gas at the solid-gas interface and 'accommodate' an assembled-azide supramolecular anion at the solid-liquid interface with crystal to crystal transformation by means of remarkable 'molecular' pathways. Interestingly, at solid-liquid interface, the interaction of azide anion with the crystal is not only driven by molecular recognition and self-assembly but also first time by anchimeric assistance. The interactions at both the interfaces stimulate new optical, magnetic, and/or ferroelectric properties, offering diversity in potential sensing application. These observations were extended to series of compounds and can add new direction in designing novel multifunctional materials, sensors or smart materials.

4.1 Crystal to Crystal transformation at Solid-Gas interface: ('Self-dissociation' and Designing strategy)

In thermal investigations of organic-inorganic hybrid materials of general type A_2CuCl_4 (where A = derivatives of aniline, benzylamine, aliphatic amines), most compounds in series lose the organic amine prior to liberation of HCl/Cl_2 gas, except that exactly opposite behavior occurs for the derivatives of benzylamine (Section 4.3.4; Figure 4.5) [5a]. The latter result suggests that a stable Cu(II)-benzylamine (and its derivatives) complex desorbs HCl gas and hence might in principle re-adsorb. To observe this latter possibility we prepared $(C_6H_5CH_2NH_2)_2CuCl_2$complex (**A_1**) (Section 4.2.2; Scheme 4.1) [6]. Single crystal X-ray study revealed that this compound has a 1-D chain structure with two equatorial Cl-Cu-Cl bridged in a trigonal pyramidal Cu(II) center (Section 4.3.5; Figure 4.6).

When these crystals were exposed to dry HCl gas, they changed colour completely (Section 4.2.2; Scheme 4.2 & Figure 4.2). The molecular structure of the resulting compound in a polycrystalline sample was established by synthesizing it as single crystals by direct reaction between $CuCl_2$ and benzilinium chloride in aqueous medium. The data summarizing crystal structure and refinement parameters are listed in Section 4.3.5; Table 4.1.

The powder-X ray pattern of the final compound matched perfectly with the powder-x-ray data simulated from the single crystal data for the A_2CuCl_4 structure **B_1** (Section 4.3.6; Figure 4.9). **B_1** crystallizes in nonpolar space group [7], with $CuCl_4^{2-}$ forming a 2-D layered structure flanked by benzylammonium cations on both the sides. We have observed similar layered structure for structurally related compounds (*p*-$ClC_6H_5CH_2NH_3)_2CuCl_4$ (B_2) [8] and $(C_6H_5CH(CH_3)NH_2CH_3)_2CuCl_4$ (B_{5S}).

Coordination complex **A_1** is stable under ambient conditions and shows change in its inner and outer coordination sphere, (Section 4.3.7;Table 4.2) after exposure to the atmosphere of hydrochloric acid vapor.

Due to a lack of pores in **A_1**, interestingly, this process requires movement of atoms in the solid state with the retention of crystallinity, a crystal to crystal transformation.Although similar observations have been made in literature, exact mechanisms have remained elusive [9].

4.2 Experimental

4.2.1 Materials and Methods:

All chemicals and solvents were of analytical grade reagents. Benzylamine and copper (II) chloride were from Aldrich; conc. hydrochloric acid (Qualigens) and ethyl alcohol (Baroda chemicals) were used without further purification.

4.2.2 Syntheses of compounds:

A general methodology of compounds preparation/syntheses is mentioned in scheme-4.1

Scheme 4.1: Synthesis of A_1

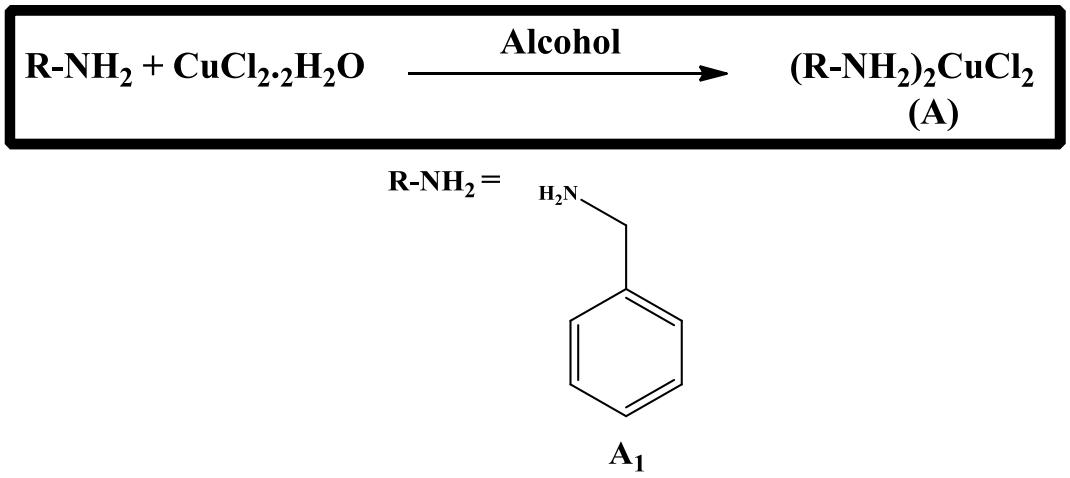

Scheme 4.2: Transformation of B_1 from A_1

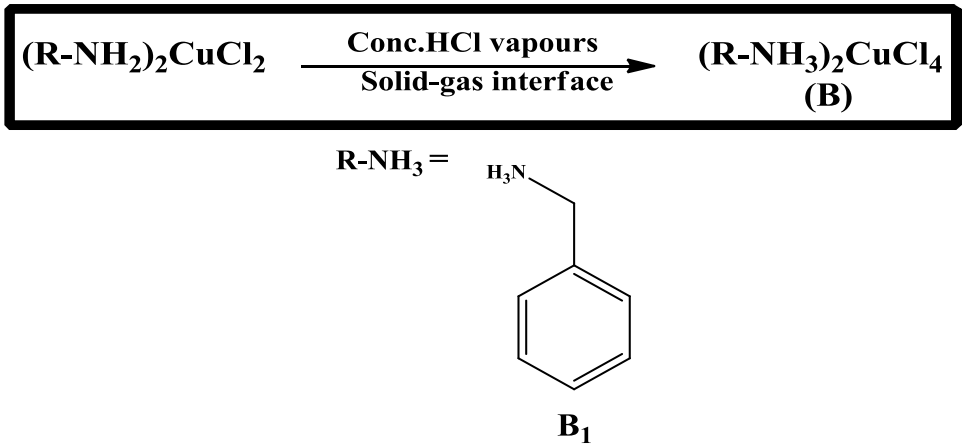

4.2.2.1 Preparation of compounds A_1

To a 3.0 mL (23.2 mmol) of benzylamine (**a_1**) in a dry 100 mL flask, 1.7048 g (10.0 mmol) $CuCl_2.2H_2O$ as added under moisture and air-free conditions. The mixture was dissolved in 30 mL of dry ethanol and refluxed for 24 h. The solvent was reduced under

vacuum causing precipitation to green solid. Slow evaporation from saturated ethanolic solution afforded 0.88 g of green crystals of $\mathbf{A_1}$. Yield:- 53.4%,

$\mathbf{A_R}$ and $\mathbf{A_S}$ were obtained using a similar method to that of $\mathbf{A_1}$, except that ligands (*R*)-(+)- ethyl phenyl amine ($\mathbf{a_{1R}}$) and (*S*)-(-)-α-methyl benzylamine ($\mathbf{a_{1S}}$) were used. Yield: 45-55%.

4.2.2.2 Preparation of dry HCl gas:

To a 50gm of $CaCl_2$ in a 500 mL flask, conc. H_2SO_4 was added drop wise (1drop HCl per min). The generated HCl gas was passed through conc. H_2SO_4 trap to eliminate the water vapours present in HCl vapors.

4.2.2.3 Transformation of B_1 from A_1.

The dry HCl gas was passed in a sample vial containing $\mathbf{A_1}$ (1 g). The reaction takes place in 2-3 hrs with observable color change to obtain $\mathbf{B_1}$ respectively.

Yield:- 100%

Fig. 4.2: Compound A_1→Compound B_1 transformation

4.3 Result and Discussions

4.3.1 FT-IR:

Figure 4.3 shows the FT-IR spectra for compound **A_1** $(C_6H_5CH_2NH_2)_2CuCl_2$ and **B_1** $(C_6H_5CH_2NH_3)_2CuCl_4$ crystals respectively at RT.

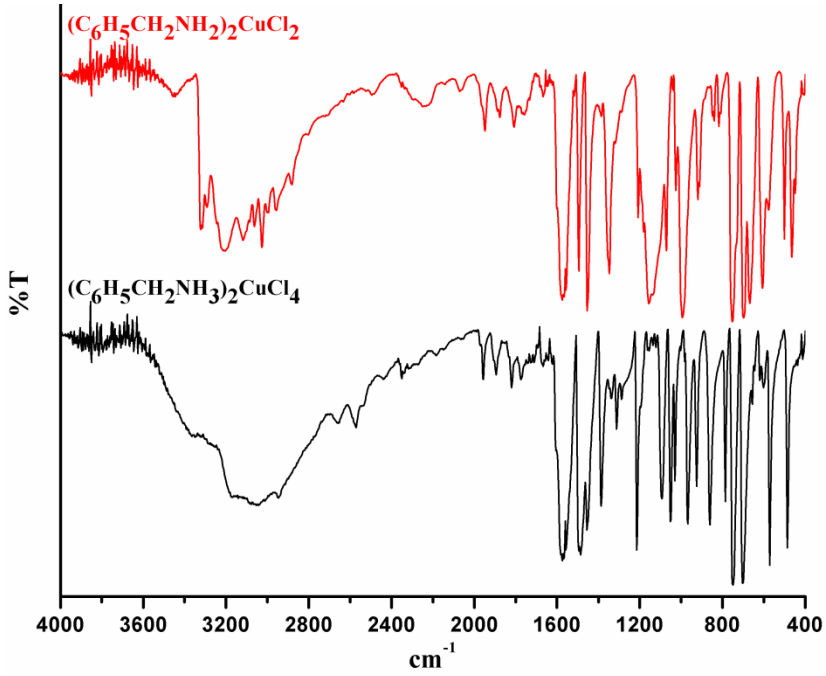

Fig. 4.3: FT-IR spectra of compound A_1 and B_1

CompoundA_1 FT-IR (KBr): 3322 (vs), 3313 (vs), 3292 (s), 3246 (m), 3210 (s), 3117 (s), 3062 (m), 3025 (s), 2997 (m), 2957 (m), 2880 (m), 2800 (w), 2068 (m), 1966 (m), 1947 (s), 1878 (m), 1804 (m), 1761 (w), 1666 (m), 1601 (s), 1575 (vs), 1555 (s), 1494 (ssh), 1387 (w), 1346 (vs), 1317 (w), 1285 (w), 1207 (m), 1181 (w), 1155 (vs), 1134 (vs), 1097 (s), 1071 (m), 1042 (w), 1024 (m), 995 (vssh), 917 (s), 908 (s), 842 (m), 819 (m), 752 (vssh), 729 (s), 697 (vs), 668 (vs), 608 (vs), 578 (s), 500 (s), 463 (vs), 448 (s) and 408 (w) cm^{-1}.

Compound B_1 FT-IR (KBr): 3154 (vs), 2885 (s), 2574 (m), 2350 (w), 2301 (w), 1958 (w), 1774 (m), 1566 (s), 1488 (s), 1456 (m), 1389 (m), 1313 (w), 1217 (s), 1098 (s), 1050 (m), 1031 (w), 968 (w), 924 (w), 864 (w), 787 (w), 754 (ssh), 701 (ssh), 669 (w), 573 (m) and 486 (m) cm^{-1}.

Symmetric and antisymmetric stretching vibrations of **A_1** were observed in range of 3289-3321 cm^{-1} and 3116-3244 cm^{-1} respectively. Stretching vibrations of NH_3 present at

3034-3174 cm^{-1}. The aromatic C-H bands in compound **A_1** were observed in range of 3024-3083 cm^{-1}. The antisymmetric -CH_2 stretching bands were observed at 2945-2997 cm^{-1} while symmetric stretching mode observed at 2881 cm^{-1} in case of **A_1**. Overtone bands were also observed in **B_1** at 2438, 2571 and 2657 cm^{-1}. Bands at the range of 1385-1496 $cm^{-1}$and 1485-1605 cm^{-1} indicate the C-C ring stretching mode. CH_2 deformation mode was observed at 1454 cm^{-1} and 1471 cm^{-1} in **B_1** while rocking modes were observed at 910-918 cm^{-1} and 923 cm^{-1} in **A_1** and **B_1** respectively.

Bands at 1315 cm^{-1} and 1623 cm^{-1} indicates the -NH_3 rocking mode and symmetric bending mode respectively in compound **B_1**. C-N stretching modes were observed at 1336 and 1346 cm^{-1}. In **A_1**, rocking mode and out of plane bending mode for -NH_2 were observed at 1155 cm^{-1} and 840-849 cm^{-1}. Bands at the range of 1026-1124 cm^{-1} corresponds to in plane CH deformation while bands at the range of 692-751 cm^{-1} correspond to out of plane phase deformation modes. Out of plane ring deformation and in plane ring deformation observed at 786 cm^{-1} and 606-619 cm^{-1} respectively.

4.3.3 Elemental analyses:

The calculated and observed elemental analyses were consistent with the formulae

CompoundA_1: Anal. Calc. for $C_{14}H_{18}Cl_2CuN_2$: C, 48.21; H, 5.20; N, 8.03%. **Found:** C, 48.11; H, 5.29; N, 7.83%.

Compound B_1: Anal. Calc. for $C_{14}H_{20}Cl_4CuN_2$: C, 39.88; H, 4.78; N, 6.61%. **Found:** C, 39.92; H, 4.70; N, 6.71%.

4.3.4 TG-DTA:

Compounds $\mathbf{A_1}$ (Figure 4.4) showed the loss of two chlorine in the range of 428-490K ((for $\mathbf{A_1}$- Obsd. 19.46 %, Calcd. 20.35 %) followed by loss of two organic ligand molecules took place. It further showed degradation pattern in the range of 491-670K (Obsd. 61.67%, Calcd. 62.02%). The remaining product at high temp is probable Cu in all compounds. The DTA curves of $\mathbf{A_1}$ indicate that the decomposition of the compound with one endothermic peak at 445.13K and one exothermic peak observed at 487K.

Compound $\mathbf{B_1}$ (Figure 4.5) is stable up to 408 K and showed mass loss of two HCl and two chlorine molecule. Compound $\mathbf{B_1}$ decomposes gradually in the range of 408-521 K (Obsd. 33.89%, Calcd. 34.01%) . Two organic ligands decomposes gradually in the range of 522-577 K for $\mathbf{B_1}$ (Obsd. 52.41%, Calcd. 50.82%) and remaining product at high temp is probable Cu (for $\mathbf{B_1}$- Obsd. 13.70%, Calcd. 15.07%).

The DTA curves of $\mathbf{B_1}$ indicate that the decomposition of the compound take place with one endothermic peak at 489 K and one exothermic peak at 527K.

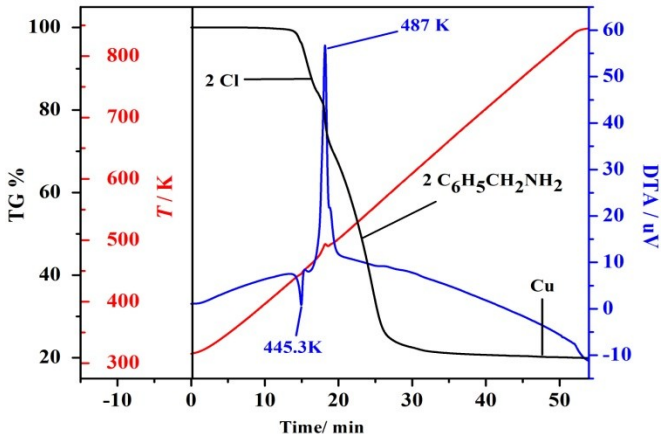

$(C_6H_5CH_2NH_2)_2CuCl_2$

2 Cl
Loss = 20.35% (calc.)
Loss = 19.46% (obsv.)
428-490K

$(C_6H_5CH_2NH_2)_2Cu$

2 $C_6H_5CH_2NH_2$
Loss = 62.02% (calc.)
Loss = 61.67% (obsv.)
491-670K

Cu
18.22% (calc.)
18.87% (obsv.)

Fig. 4.4: TG/DTA curve and degradation pattern for compounds A_1

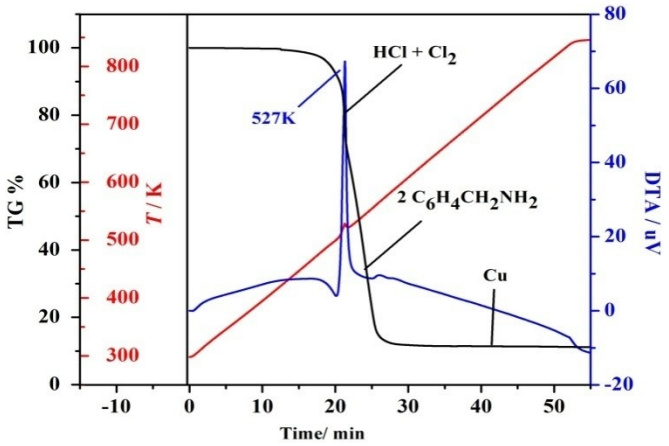

$(C_6H_5CH_2NH_3)_2CuCl_4$

2HCl + Cl_2
Loss = 34.01% (calc.)
Loss = 33.89% (obsv.)
408-521K

$(C_6H_5CH_2NH_2)_2Cu$

2 $C_6H_5CH_2NH_2$
Loss = 50.82% (calc.)
Loss = 52.41% (obsv.)
522-577K

Cu
15.07% (calc.)
13.70% (obsv.)

Fig. 4.5: TG/DTA curve and degradation pattern for compounds B_1

4.3.5 Single Crystal X-ray Diffraction

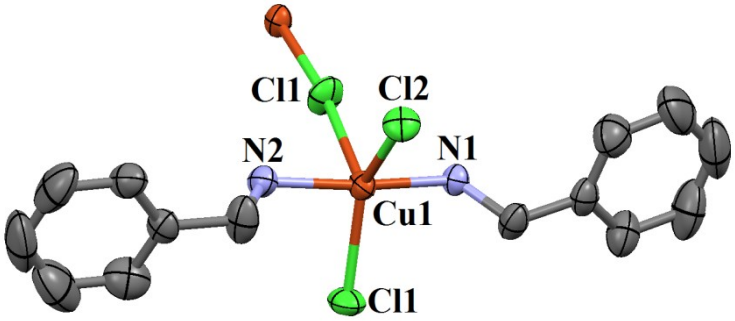

Fig. 4.6: Molecular view of A_1(thermal ellipsoid are shown at 50 % probability)

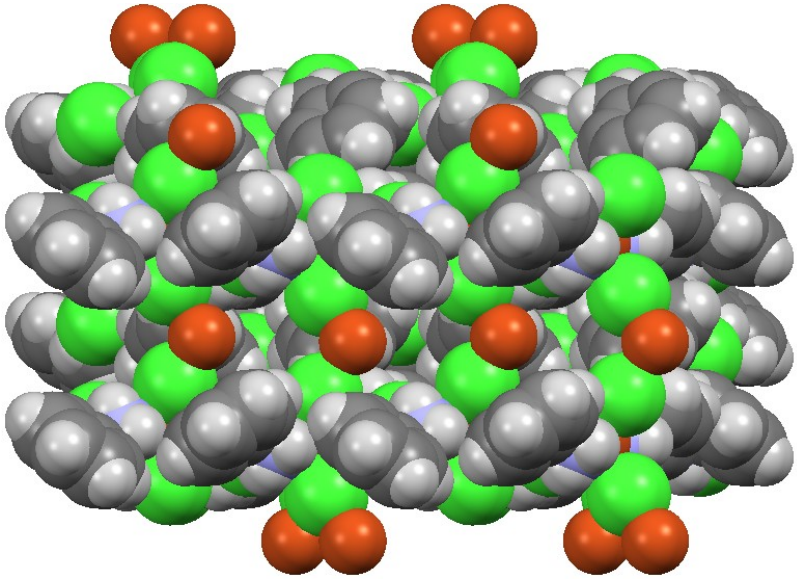

Fig. 4.7: Molecular view of (a) A_1 and (b) A_1 with space filled style denotes the absence of porosity

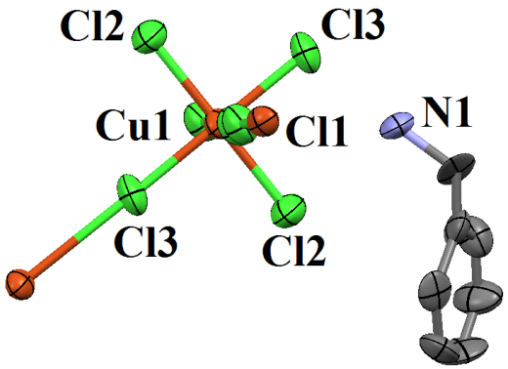

Fig. 4.8: Molecular view of B_1 (thermal ellipsoid are shown at 50 % probability)

Table 4.1: X-ray crystal data of B_1

	A_1	B_1
CCDC	**608611**	**1015762**
Empirical formula	$C_{14}H_{18}Cl_2Cu_2N_2$	$C_{28}H_{40}Cl_8Cu_2N_4$
Formula weight	348.74	843.32
Temperature/K	294(2)	100(2)
Crystal system	Orthorhombic	Triclinic
Space group	*Pbca*	*P*1
a (Å)	8.2260(8)	10.4498(12)
b (Å)	12.4900(11)	10.4921(12)
c (Å)	31.207(3)	15.9114(18)
α(°)	90.00	81.218(3)
β(°)	90.00	80.432(3)
γ(°)	90.00	89.237(3)
V (Å3)	3206.3(5)	1700.0(3)
Z	8	2
Dcalc (Mg/m^3)	1.445	1.648
Reflections collected	18381	20181
Independent reflections	3957 [R_{int} = 0.0405, R_{sigma}= 0.0294]	11016 [R_{int} = 0.0491, R_{sigma}= 0.0839]
Goodness-of-fit on F^2	1.183	0.908
Data / restraints / Parameters	3957/0/172	11016/114/663
Final R indices [I>2α(I)]	R_1 = 0.0546, wR_2 = 0.1220	R_1 = 0.0771, wR_2 = 0.2121
R indices (all data)	R_1 = 0.0692, wR_2 = 0.1295	R_1 = 0.1067, wR_2 = 0.2373

4.3.6 Powder X-ray diffraction:

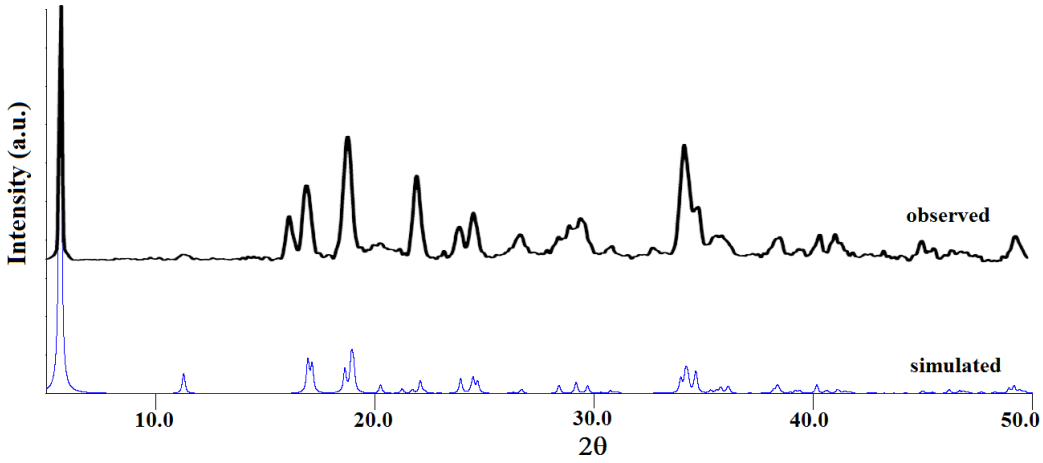

Fig. 4.9: Observed and Simulated Powder X-Ray Diffraction Patterns of B_1

4.3.7 Inner coordination and outer coordination sphere

Table 4.2: Bond lengths of A_1 and B_1

	A_1 (Å)	B_1 (Å)
Cu (1)-N(1)	1.983(3)	
Cu (1)-N(2)	1.984(3)	
Cu (1)-Cl(1)	2.340(11)	2.289(2)
Cu (1)-Cl(1#)	2.629(11)	2.289(2)
Cu (1)-Cl(2)		2.293(2)
Cu (1)-Cl(2#)		2.298(2)
Cu (1)-Cl(3)	2.299(10)	

4.4 Crystal to Crystal transformation Solid-Gas interface: (Probing Mechanism)

The chemisorption of HCl occurs with dramatic colour change from dark green (**A_1**) to yellow (**B_1**) over 30 to 150 minutes in 100% yield, as demonstrated unequivocally by *ex-situ* monitoring using FT-IR (Section 4.4.1; Figure 4.10) and XRPD (Section 4.4.2; Figure 4.11). This transformation happens in two main steps, which we propose to occur mechanistically as shown in Section 4.4.3; Figure 4.12 [10].

In the first step due to chemisorption of HCl gas, benzylamine changes its role from ligand (inner coordination sphere) to counter cation (outer coordination sphere) with formation of benzylammonium cation at the cost of breaking all covalent Cu–N and H–Cl bonds Section 4.4.3; Figure 4.12b. This means 'self-dissociation' of HCl gas into H^+ cation and Cl^- anion is triggering this step. This is observed clearly in FT-IR by the gradual decrease in intensity of vibrations attributable to free amine and formation of ammonium moiety features. XRPD also reveals that the changes occur in the planes where (benzylamine) C-N atoms are located (Section 4.4.3; Table 4.3). This process it complete in about 60 minutes [11]. The addition of base (KOH) inserts benzylamine backinto the inner coordination sphere from a counter cation position, by abstracting a proton, as cleanly seen in FT-IR and powder X-ray (Section 4.4.4; Figure 4.13).

The second step in the overall transformation of Figures 4.10-4.11 is most crucial, where the accommodating ability of Cu(II) allows a change in hybridization from $(d^2)sp^2$ to dsp^2 with a cross-dimeric eight (8) membered ring formation (analogous to the classical example of $AlCl_3$ compared to Al_2Cl_6), where bonds are formed between Cu(II) and a neighboring unbound -Cl (*p*-orbital) atom attached to another Cu(II) atom in a 1-D chain (Section 4.4.3; Figure 4.12-c,d). This means charge neutrality is achieved for the1-D $[CuCl_3]^{1-}_n$ chain by extending its growth at the chain boundary interface to form a layered structure with nearly perfect squares of $[Cu_4Cl_4]_n$units. Interestingly, an inversion center is observed exactly between these 1-D layers on the {028} plane ($2\theta = 26°$), (shown by orange colour in Section 4.4.3; Figure 4.12c) which diminishes during the process of HCl accommodation.

4.4.1 *ex-situ* Reaction Monitoring using FT-IR

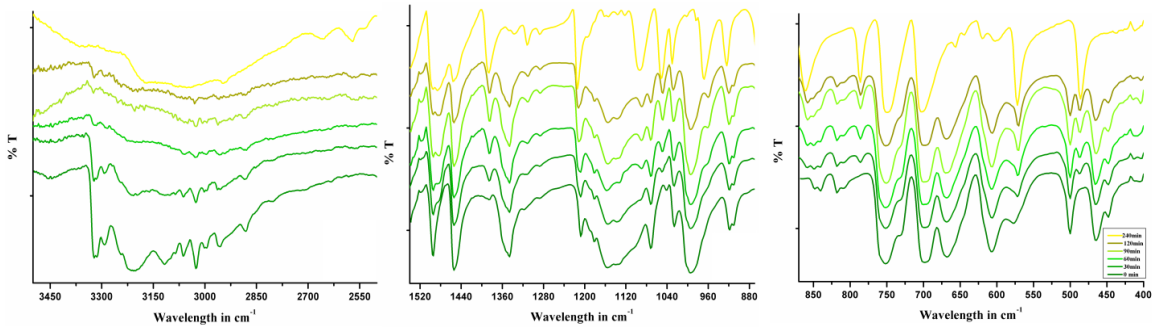

Fig. 4.10: FT-IR study: Monitoring of HCl gas adsorption with time during transformation of A_1 to B_1. (colour of the spectra are matching with the colour of the sample during this transformation)

4.4.2 *ex-situ* reaction monitoring using Powder X-ray diffraction

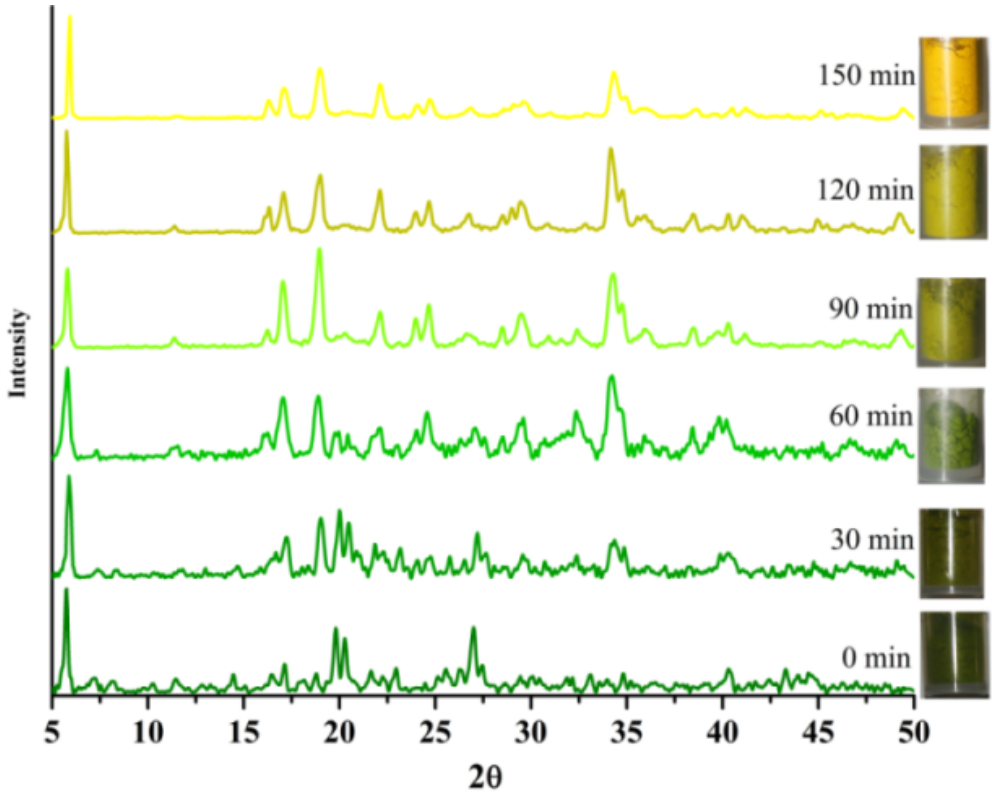

Fig. 4.11: Powder X-ray study: Monitoring (*ex-situ*) of HCl gas adsorption with time during transformation of A_1 to B_1. (colour of the spectra are matching with the colour of the sample during this transformation)

4.4.3 Probable Mechanism of transformation of A_1 to B_1

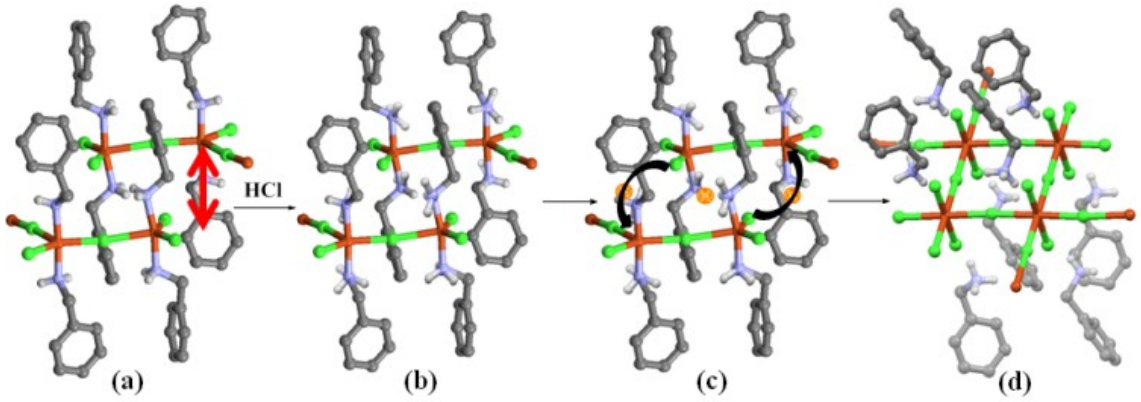

Fig. 4.12: Probable mechanism for transformation of (a) 1-D chain of A_1 to (d) 2-D layer of B_1 through (b) benzylammonium formation, and (c) charge neutrality driven layer formation at the expense of inversion center between the layers

Table 4.3: Planes {h k l} passing through different 2θ values in A_1

Entry No.	2θ (°)	*h k l*	Plane passing through
1	16.53	0 2 3	amine nitrogen
2	17.03	0 0 6	phenyl rings and parallel to *ab*-axis
3	18.70	1 2 2	amine nitrogen and bridged chlorine
4	19.74	1 2 3	amine nitrogen and bridged chlorine
5	20.19	1 0 6	benzyl carbon
6	26.93	0 2 8	amine nitrogen and parallel to two 1D Cu-Cl chain and on inversion centre
7	29	1 2 8	amine nitrogen, bridged chlorine and benzyl carbon
8	33.85	1 4 5	phenyl rings and Cu-N-Cu
9	34.62	3 0 4	Cu-N
10	38.60	1 5 3	Cu and amine group
11	49.36	2 6 2	amine nitrogen and bridged chlorine

4.4.4 Powder X-ray diffraction

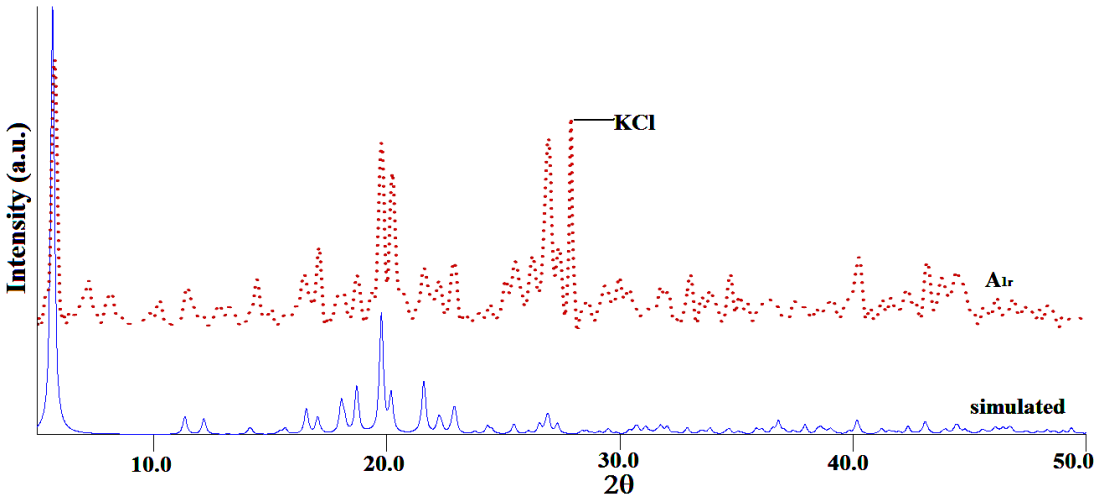

Fig. 4.13: Observed (KOH treatment-A_{1r}) and Simulated Powder X-Ray Diffraction Patterns of A_1 (Note the peak due to eliminated KCl at 2θ=28°)

4.5 Accommodative processes at a Solid-Gas interface: Stereochemistry of Crystal to Crystal transformations

The above mechanism would not provide detectable stereochemical changes during the transformation of $\mathbf{A_1}$ to $\mathbf{B_1}$. Therefore, we synthesized (Section 4.5.2; Scheme 4.3) a pair of enantiomerically pure complexes (((*R*)-(+)-*α*-ethyl phenyl amine)$_2$CuCl$_2$ ($\mathbf{A_R}$) and ((*S*)-(-)-*α*-ethyl phenyl amine)$_2$CuCl$_2$ ($\mathbf{A_S}$))and their respective double salts (Section 4.5.2; Scheme 4.4) (((*R*)-(+)-*α*-ethyl phenyl ammonium)$_2$CuCl$_4$ ($\mathbf{B_R}$) and ((*S*)-(-)-*α*-ethyl phenyl ammonium)$_2$CuCl$_4$ ($\mathbf{B_S}$)), using *α*-ethyl phenyl amine as a chiral ligand.

Single crystal X-ray revealed that paired $\mathbf{A_R}$-$\mathbf{A_S}$ and $\mathbf{B_R}$-$\mathbf{B_S}$ have similar structures but not 1-D chains (similar to $\mathbf{A_1}$) or 2-D layered structure (similar to $\mathbf{B_1}$). $\mathbf{A_R}$ crystallizes in the monoclinic chiral space group *P*1 at RT (Section 4.5.6.1; Figure 4.18a) as a dinuclear complex with long sheared Cu-Cl bonds between two slightly distorted square planar Cu(II) centers. No prominent hydrogen bonding interactions or lattice porosity was observed in its crystal packing. $\mathbf{B_R}$ crystallizes in the monoclinic chiral space group C_2 at RT (Section 4.5.6.1; Figure 4.19a) with isolated highly distorted tetrahedral geometry around $CuCl_4^{2-}$anions (Cl-Cu-Cl trans angle 152.21º), with three N–H···Cl (3.180(2) Å) hydrogen bonds and two bifurcated 2(N–H)···Cl (3.228(3) and 3.235(1)Å) hydrogen bonds. The data summarizing crystal structure and refinement parameters are listed in Section 4.5.6.1; Table 4.4.

$\mathbf{A_R}$/$\mathbf{A_S}$ also absorbs HCl gas to give a crystal to crystal transformation to $\mathbf{B_R}$/$\mathbf{B_S}$ like that in Figure 4.1 and Section 4.5.6.1; Figure 4.14. After chemisorption, the unit cell volume of $\mathbf{B_R}$/$\mathbf{B_S}$ increased by 16% with reduction in the crystal packing index (*Z*) from 1 to 2. This transformation was monitored using UV-vis. (Section 4.5.7; Figure 4.20), FT-IR (Section 4.5.8; Figure 4.21), Powder XRD (Section 4.5.9; Figure 4.22 & 4.23), cyclic dichroism (CD) spectra (Section 4.5.10; Figure 4.25 & 4.26), and Specific Optical Resolution activity (Section 4.5.11; Table 4.6 & 4.7).

Figure 4.26 shows no change in Cotton effect for CD spectroscopic study during chemisorption of HCl and desorption by grinding with KOH pellets. This process gave no change in optical rotation or SOR activity, confirming conservation of enantiomerism during these reversible structural changes (Section 4.5.11; Table 4.6 & 4.7).

Thus, one can say that substitution occurs associatively in the crystal. This may be the reason for the observed sustainability of crystalline character during this transformation. This also would explain occurrence of spin density only on Cu and Cl atoms, and not on amine N atom, during preliminary DFT investigation on the complex and double salt (Section 4.5.12; Figure 4.27).

The results suggest that one can design molecular complexes with reversible sorption-desorption or accommodative behaviorby simply observing the thermal degradation pathway, as shown for set of compounds in this article as (Section 4.5.13; Figure 4.28).

In literature work to date, most similar molecules have been studied using TGA, but no emphasis was put on this analysis from designing perspective for accommodative type of compounds.

4.5.1 Materials and Methods:

All chemicals and solvents were of analytical grade reagents. (*R*)-(+)-*α*-methyl benzylamine, (*S*)-(-)-*α*-methyl benzylamine and copper (II) chloride were from Aldrich; conc. hydrochloric acid (Qualigens) and ethyl alcohol (Baroda chemicals) were used without further purification.

4.5.2 Syntheses of compounds:

A general methodology of compounds preparation/syntheses is mentioned in scheme-4.3 [12].

Scheme 4.3: Synthesis of A_R/A_S

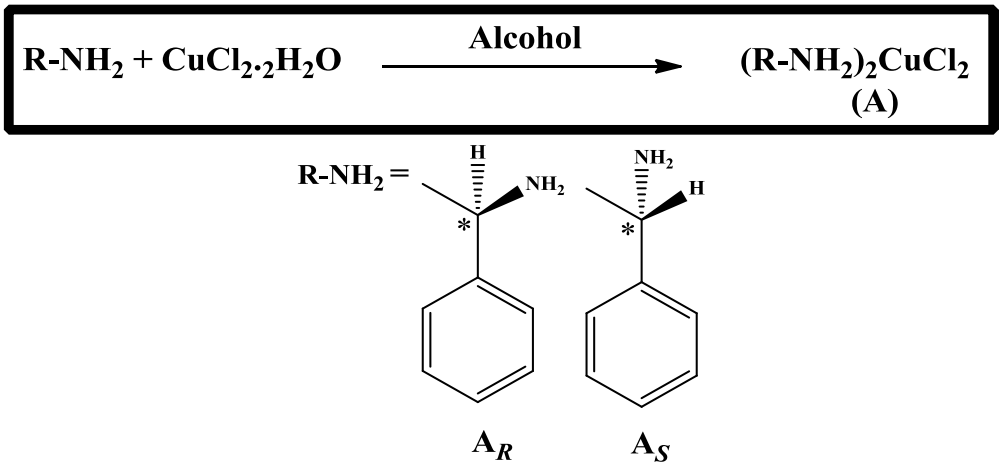

Compound A_R:$[a]_D^{25}$ =+81.78 (c 0.0428, THF) for ((*R*)-(+)-*α*-ethyl phenyl amine)$_2$CuCl$_2$.

Compound A_S: $[a]_D^{25}$ = -81.71 (c 0.0428, THF) for ((*S*)-(-)-*α*-ethyl phenyl amine)$_2$CuCl$_2$.

Scheme 4.4: Transformation of B_R/B_S from A_R/A_S

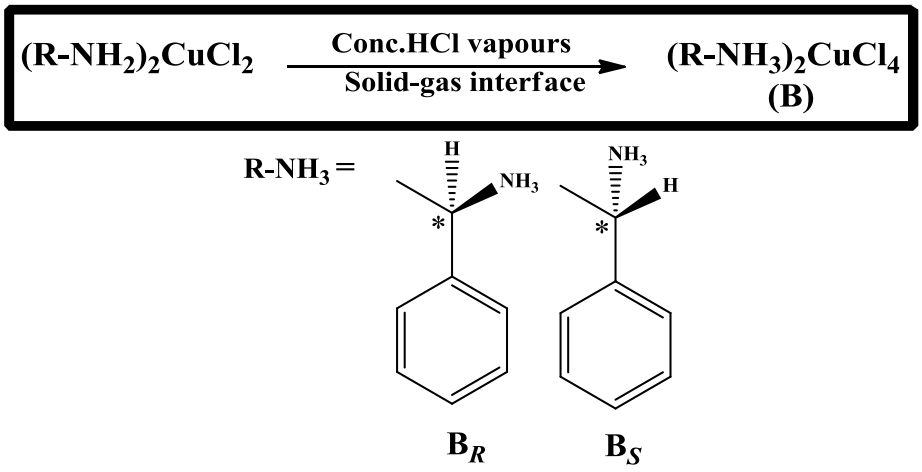

4.5.2.1 Preparation of compounds A1

The dry HCl gas was passed in a sample vial containing $\mathbf{A_R/A_S}$ (1 g). The reaction takes place in 2-3 hrs with observable color change to obtain $\mathbf{B_R/B_S}$ respectively.

Yield:- 100%

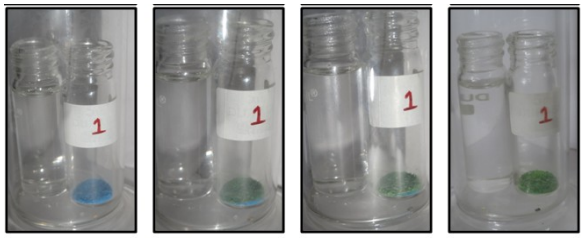

Fig. 4.14: Compound A_R / A_S → Compound B_R / B_S transformation

4.5.3 FT-IR:

Figure 4.15 shows the FT-IR spectra of compound $\mathbf{A_R/A_S}$ $(C_6H_5CH(CH_3)NH_2)_2CuCl_2$, $\mathbf{B_R/B_S}$ $(C_6H_5CH(CH_3)NH_3)_2CuCl_4$ crystals at RT. It is observed that stretching vibration bands of NH_3^+ were present at 3028-3055 cm^{-1} in $\mathbf{B_R/B_S}$ while that of $-NH_2$ symmetric and antisymmetric stretching observed in the range of 3306-3325 cm^{-1} and 3216-3249 cm^{-1} for $\mathbf{A_R/A_S}$. Aliphatic $-CH_3$ stretching band observed at 2973 cm^{-1} in $\mathbf{A_R/A_S}$ while $-CH_3$ symmetric deformation mode observed in all compounds in the range 1385-1374 cm^{-1} and at 1290 cm^{-1}.

A band at 1622 cm^{-1} and 1315 cm^{-1} indicates the $-NH_3$ symmetric bending mode and rocking mode in compound $\mathbf{B_R/B_S}$. C-H ring stretching modes were observed in range of 1455-1604 cm^{-1} in all compounds. Bands in the range of 1336-1340 cm^{-1} indicate the C-N stretching mode. $-NH_2$ rocking mode was observed in the range 1152-1159 cm^{-1} and out of plane bending mode observed at 847 cm^{-1} in $\mathbf{A_R/A_S}$. *in- plane* CH deformation modes were observed in the range 1028-1240 cm^{-1} while out-of-plane deformation modes in the range 698-747 cm^{-1}. C-C *stretching* mode was observed in the range 970-994 cm^{-1}. Bands in the range 910-916 cm^{-1} was attributed to $-CH_2$ *rocking* mode. Sharp bands were observed at 749-770 cm^{-1} assigned to the *out-of- plane* ring deformation.

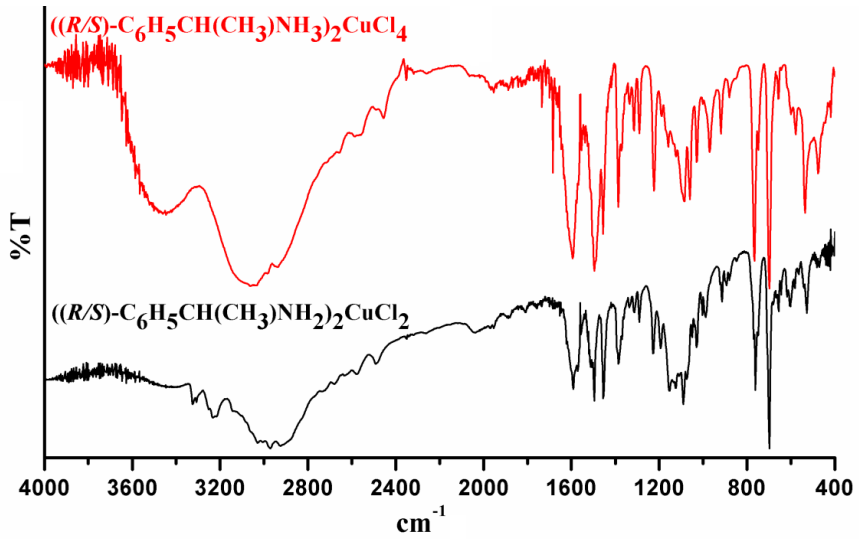

Fig. 4.15: FT-IR spectra of compound A_R /A_S and B_R / B_S

Compound A_R FT-IR (KBr): 3321 (m), 3301 (s), 3250 (w), 3220 (s), 3025 (vs), 2966 (vs), 2916 (s), 2722 (w), 2772 (w), 2765 (m), 2480 (s), 2032 (m), 1971 (w), 1951 (w), , 1887 (w), 1810 (w), 1589 (vs), 1568 (s), 1516 (s), 1496 (ssh), 1456 (ssh), 1383 (vs), 1336 (w), 1291 (m), 1226 (s), 1193 (s), 1155 (vs), 1126 (s), 1090 (vs), 1071 (s), 1028 (m), 1007 (w), 986 (m), 917 (m), 891 (w), 875 (w), 772 (s), 764 (s), 749 (s), 699 (vssh), 656 (w), 604 (m), 580 (w) and 528 (m) cm^{-1}.

Compound A_S FT-IR (KBr): 3322 (s), 3303 (m), 3250 (w), 3222 (s), 3140 (w), 3026 (vs), 2968 (vs), 2915 (s), 2720 (w), 2772 (w), 2767 (m), 2481 (s), 2031 (m), 1971 (w), 1952 (w), , 1885 (w), 1810 (w), 1591 (vs), 1567 (s), 1516 (s), 1495 (ssh), 1456 (ssh), 1384 (vs), 1336 (w), 1315 (w), 1291 (m), 1228 (s), 1194 (s), 1153 (vs), 1126 (s), 1089 (vs), 1071 (s), 1051 (w), 1029 (m), 1005 (w), 987 (m), 915 (m), 891 (w), 879 (w), 770 (s), 761 (s), 749 (s), 698 (vssh), 656 (w), 617 (w), 604 (m), 583 (w) and 527 (m) cm^{-1}.

Compound B_R FT-IR (KBr): 2946 (vs), 2656 (m), 1593 (vs), 1564 (s), 1494 (vs), 1454 (vs), 1386 (vs), 1370 (m), 1334 (w) 1314 (m), 1288 (m), 1222 (vs), 1161 (m), 1083 (s), 1058 (s), 1029 (m), 970 (s), 918 (m), 766 (vssh), 749 (m), 697 (vssh), 536 (vssh) and 476 (m) cm^{-1}.

Compound B_S FT-IR (KBr): 3054 (vs), 2656 (m), 1593 (vs), 1564 (s), 1493 (vs), 1454 (vs), 1386 (vs), 1370 (m), 1334 (w), 1314 (m), 1288 (m), 1222 (vs), 1161 (m), 1083 (s), 1058 (s), 1029 (m), 970 (s), 918 (m), 766 (vssh), 749 (m), 697 (vssh), 537 (vssh) and 476 (m) cm^{-1}.

4.5.4 Elemental analyses:

The calculated and observed elemental analyses were consistent with the formulae

Compound A_R:Anal. Calc. for $C_{16}H_{22}N_2CuCl_2$: C, 50.73; H, 6.39; N, 7.39%.**Found:** C, 50.79; H, 6.26; N, 7.43%.

Compound A_S:Anal. Calc. for $C_{16}H_{22}N_2CuCl_2$: C, 50.73; H, 6.39; N, 7.39%. **Found:** C, 50.76; H, 6.31; N, 7.34%.

Compound B_R:Anal. Calc. for $C_{16}H_{24}N_2CuCl_4$: C, 42.73; H, 5.38; N, 6.23%. **Found:** C, 42.69; H, 5.28; N, 6.18%.

Compound B_S: Anal. Calc. for $C_{16}H_{24}N_2CuCl_4$: C, 42.73; H, 5.38; N, 6.23%. **Found:** C, 42.42; H, 5.44; N, 6.28%.

4.5.5 TG-DTA

4.5.5.1 TG-DTA of compounds A_R and A_S

Compound $\mathbf{A_R}$ (Figure 4.16a) and $\mathbf{A_S}$ (Figure 4.16b) showed similar decomposition pattern. Compounds $\mathbf{A_R}$ and $\mathbf{A_S}$ showed the loss of two chlorine in the range of 390-440K ((for $\mathbf{A_R}$ - Obsd. 19.06 %, Calcd. 18.93 %), (for $\mathbf{A_S}$ - Obsd. 19.86 %, Calcd. 18.93 %)) respectively followed by the loss of two organic ligand molecules. Compound $\mathbf{A_R}$ (Obsd. 64.12%, Calcd. 65.16%) and $\mathbf{A_S}$ (Obsd. 63.09%, Calcd. 65.16%) decomposes in the range of 440-790K and remaining product at high temp is probable Cu in all compounds. The DTA curves of $\mathbf{A_R}$, and $\mathbf{A_S}$ indicate that the decomposition of the compound with one endothermic peak at 417.4K and 417.4K respectively and one exothermic peak observed at 514K and 470K respectively.

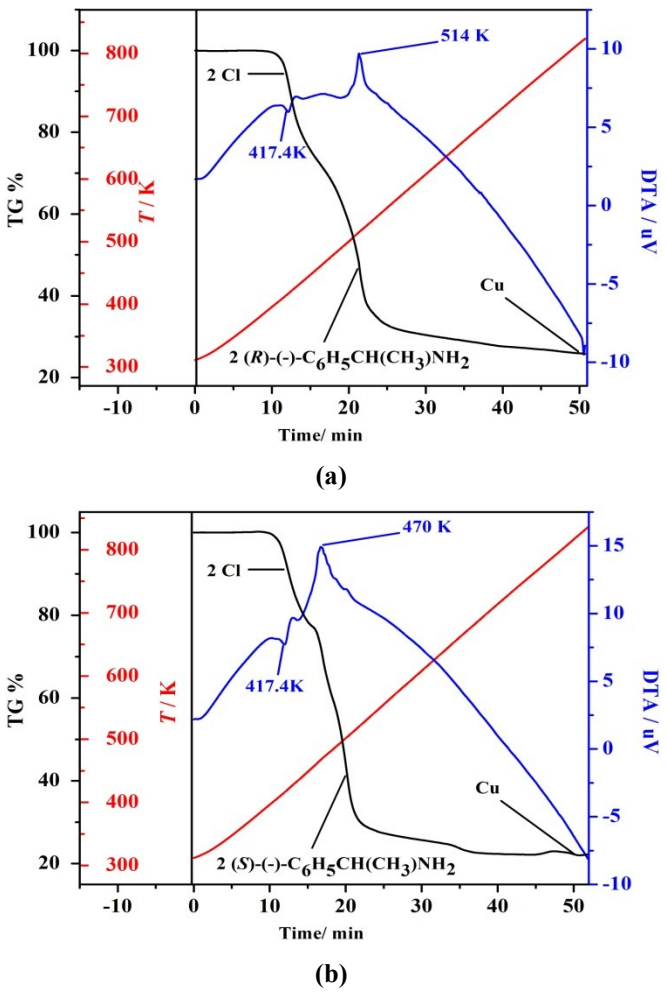

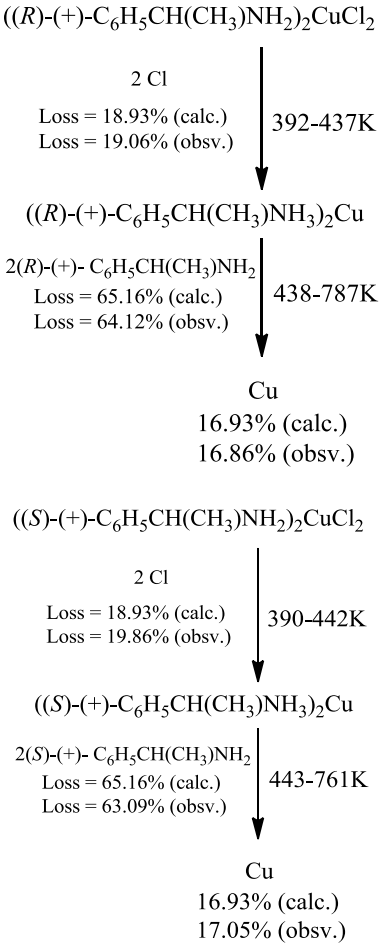

Fig. 4.16: TG/DTA curve and degradation pattern for compounds A_R (a) and A_S (b)

4.5.5.2 TG-DTA of compounds B_R and B_S

The multistep decomposition patterns of compound $\mathbf{B_R}$ (Figure 4.17a) and $\mathbf{B_S}$ (Figure 4.17b) are very similar. Compound $\mathbf{B_R}$ and $\mathbf{B_S}$ are stable up to 430 K and showed mass loss of two HCl and two chlorine molecule. Compound $\mathbf{B_R}$ (Obsd. 31.18%, Calcd. 31.98%) and $\mathbf{B_S}$ (Obsd. 31.03%, Calcd. 31.98%) decomposes in the range of 430-499K. Two organic ligands decomposes gradually in the range of 500-756 K for $\mathbf{B_R}$ (Obsd. 53.32%, Calcd. 53.89%) and 493-795 K for $\mathbf{B_S}$ (Obsd. 54.01%, Calcd. 53.89%). The remaining product at high temp is probable Cu (for $\mathbf{B_R}$ - Obsd. 15.52%, Calcd. 14.13%) and (for $\mathbf{B_S}$ - Obsd. 14.96%, Calcd. 14.13%). The DTA curves of $\mathbf{B_R}$ and $\mathbf{B_S}$ indicate that the decomposition of the compound take place with one endothermic peak at 448.4K and 449.4K respectively. Two exothermic effects (crystallization, desolvation/dehydration) were observed at 484.4 K and 507 K in case of $\mathbf{B_R}$ and 484.2K and 504K in case of $\mathbf{B_S}$.

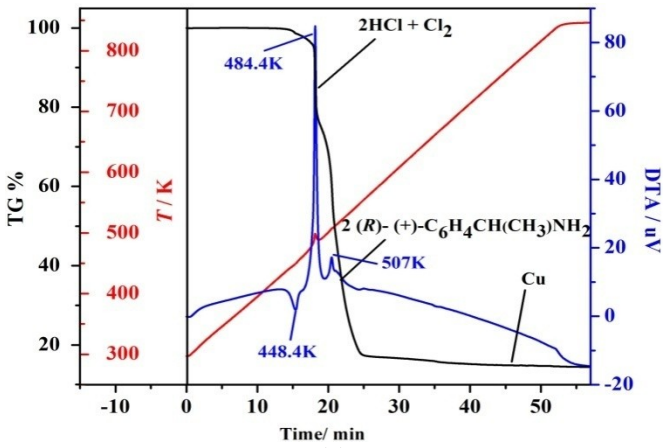

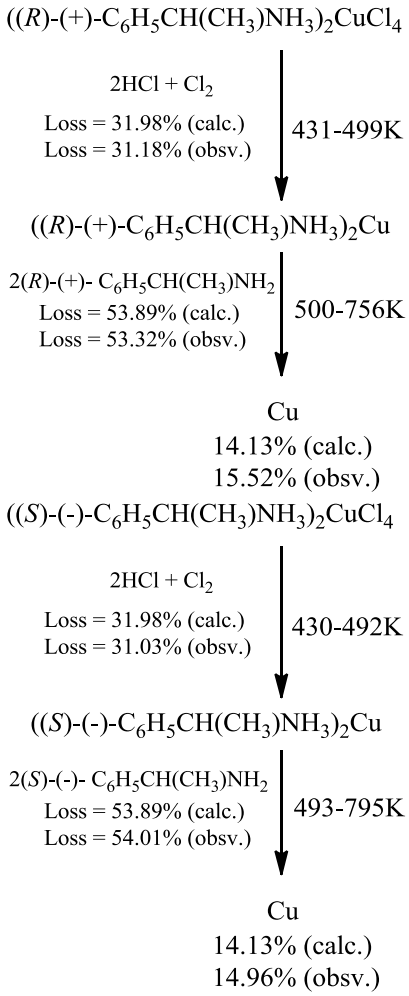

Fig. 4.17: TG/DTA curve and degradation pattern for compounds B_R (a) and B_S (b)

4.5.6 Crystal structure

4.5.6.1 Single Crystal X-ray Diffraction A_R and A_S

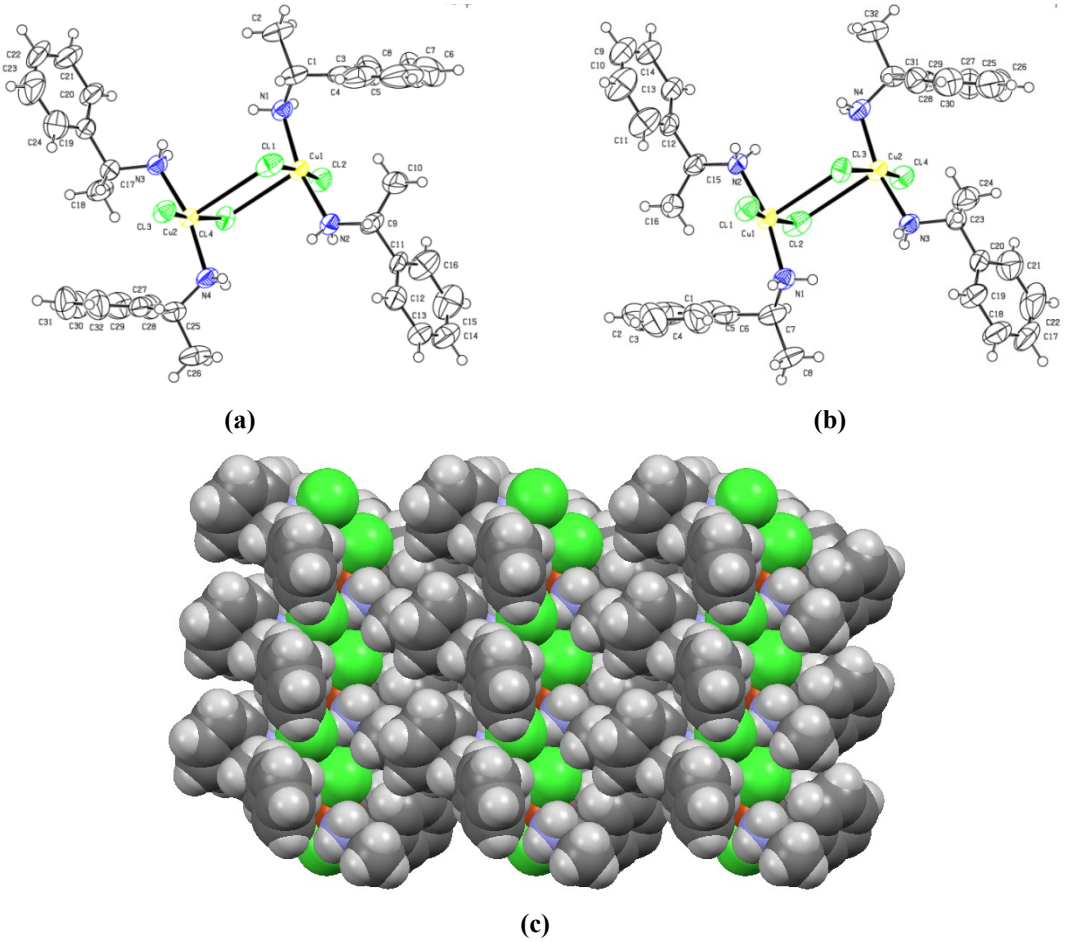

(a) **(b)**

(c)

Fig. 4.18: Molecular view of (a) A_R and (b) A_S (thermal ellipsoid are shown at 50 % probability); (c) A_R with space filled style denotes the absence of porosity

4.5.6.2 Single Crystal X-ray Diffraction A_R and A_S

B_R ((*R*)-(+)-Me-benzilinium)$_2$CuCl$_4$ and **B_S** ((*S*)-(-)-Me-benzilinium)$_2$CuCl$_4$ crystallized into monoclinic crystal system with C_2 space group. Here $[CuCl_4]^{2-}$ dianions are surrounded by organic ammonium cations and stabilized by hydrogen bonding interaction. Three N–H···Cl (3.180(2) Å) hydrogen bond and two bifurcated 2(N–H)···Cl (3.228(3) and 3.235(1)Å) hydrogen bonds were observed.

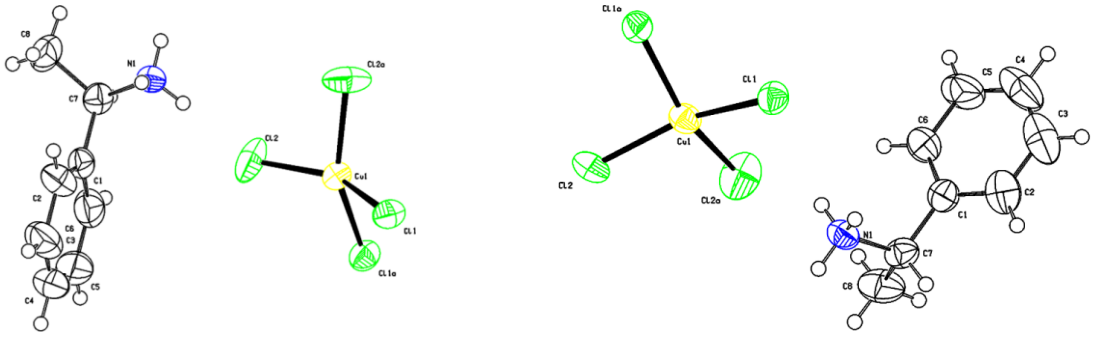

(a) (b)

Fig. 4.19: Molecular view of (a) B_R and (b) B_S (thermal ellipsoid are shown at 50 % probability)

Table 4.4: Crystallographic data and structure refinements for s B_R and B_S at RT

	B_R	B_S
CCDC	**817150**	**817151**
Empirical formula	$C_{16}H_{24}Cl_4CuN_2$	$C_{16}H_{24}Cl_4CuN_2$
Formula weight	449.71	449.71
Wavelength (Å)	0.71073	0.71073
Crystal system	Monoclinic	Monoclinic
Space group	C_2	C_2
a (Å)	10.567(3)	10.582(3)
b (Å)	7.253(2)	7.257(2)
c (Å)	13.926(4)	13.940(3)
β(°)	95.99(3)	96.04(2)
V (Å3)	1061.5(5)	1064.5(5)
Z	2	2
Dcalc (Mg/m^3)	1.407	1.403
Reflections collected	2266	2263
Independent reflections	1848 [*R*int = 0.0185]	1688 [*R*int = 0.0209]
Goodness-of-fit on F^2	1.031	0.974
Data / restraints / Parameters	1848 / 1 / 105	1688 / 1 / 105
Final R indices [I>2α(I)]	R1 = 0.0324, wR2 = 0.0685	R1 = 0.0346, wR2 = 0.0633
R indices (all data)	R1 = 0.0404, wR2 = 0.0750	R1 = 0.0438, wR2 = 0.0689

4.5.6.3 Inner coordination and outer coordination sphere

Tables 4.5: Bond lengths of A_R, A_S, B_R and A_S

	A_R (Å)	B_R (Å)	A_S (Å)	B_S (Å)
Cu(1)-Cl(1)	2.295(17)	2.264(9)	2.292(16)	2.269(11)
Cu(1)-Cl(1#)	2.317(17)	2.264(9)	2.319(16)	2.269(11)
Cu(1)-Cl(2)		2.239(11)		2.239(12)
Cu(1)-Cl(2#)		2.239(11)		2.239(12)
Cu(1)-Cl(3)	2.828(2)		2.836(2)	
Cu(2)-Cl(2)	2.285(16)		2.286(16)	
Cu(2)-Cl(2#)	2.285(17)		2.282(15)	
Cu (1)-N(1)	2.001(5)		2.015(3)	
Cu (1)-N(2)	2.010(5)		1.997(3)	

4.5.7 Solid state absorption spectra:

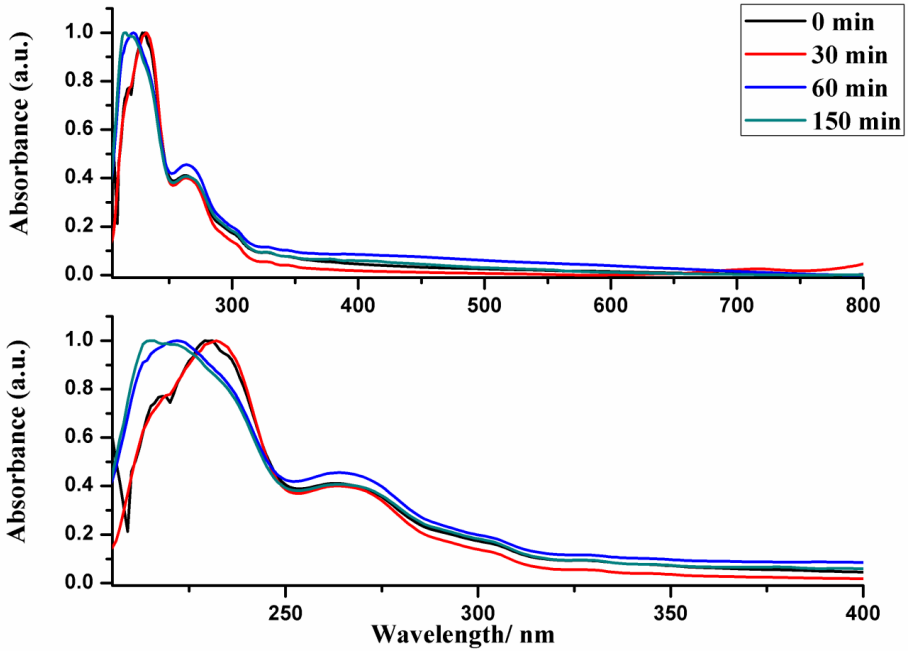

Fig. 4.20: Solid state absorption spectra of conversion of $A_S \rightarrow B_S$

The electronic spectra of $\mathbf{A_S}$ showed the absorbance maxima at 230nm as shown in Figure 4.20. It does not showed any sign of *d-d* transition. After 30 min. exposure with HCl, *d-d* transitions band centered around 717 nm observed a five- coordinate copper(II) environment. The electronic spectra of copper (II) complexes with square-pyramidal geometries have been studied extensively by Hathaway and coworkers [13]. It was possible to predict the stereochemistry of the local copper (II) ion environment in five-coordinated complexes from the positions and intensities of the d-d transition bands of CuX5 chromophores. The electronic spectra of distorted square-based pyramidal complexes consist of a single or two bands covering the range 667 ±50nm [14]. This distortion is towards a tetrahedral arrangement of the basal plane. The position of the *d-d* band in $\mathbf{A_S}$ is very similar to that reported for the copper(II) complexes in which copper(II) atoms have a distorted tetrahedral-based pyramidal geometry suggesting the addition of chlorine atom to copper metal.

After 60 minutes exposure to HCl vapours, showed hypsochromic and hypochromic shift in the spectra. The spectra of complex showed strong band around 221nm suggesting that formation of $\mathbf{B_S}$. No sign of d-d transition was observed at this stage. At 150 min. more hypsochromic shift 214nm in the spectra confirms the formation $\mathbf{B_S}$ from $\mathbf{A_S}$.

4.5.8 *ex-situ* reaction monitoring using FT-IR

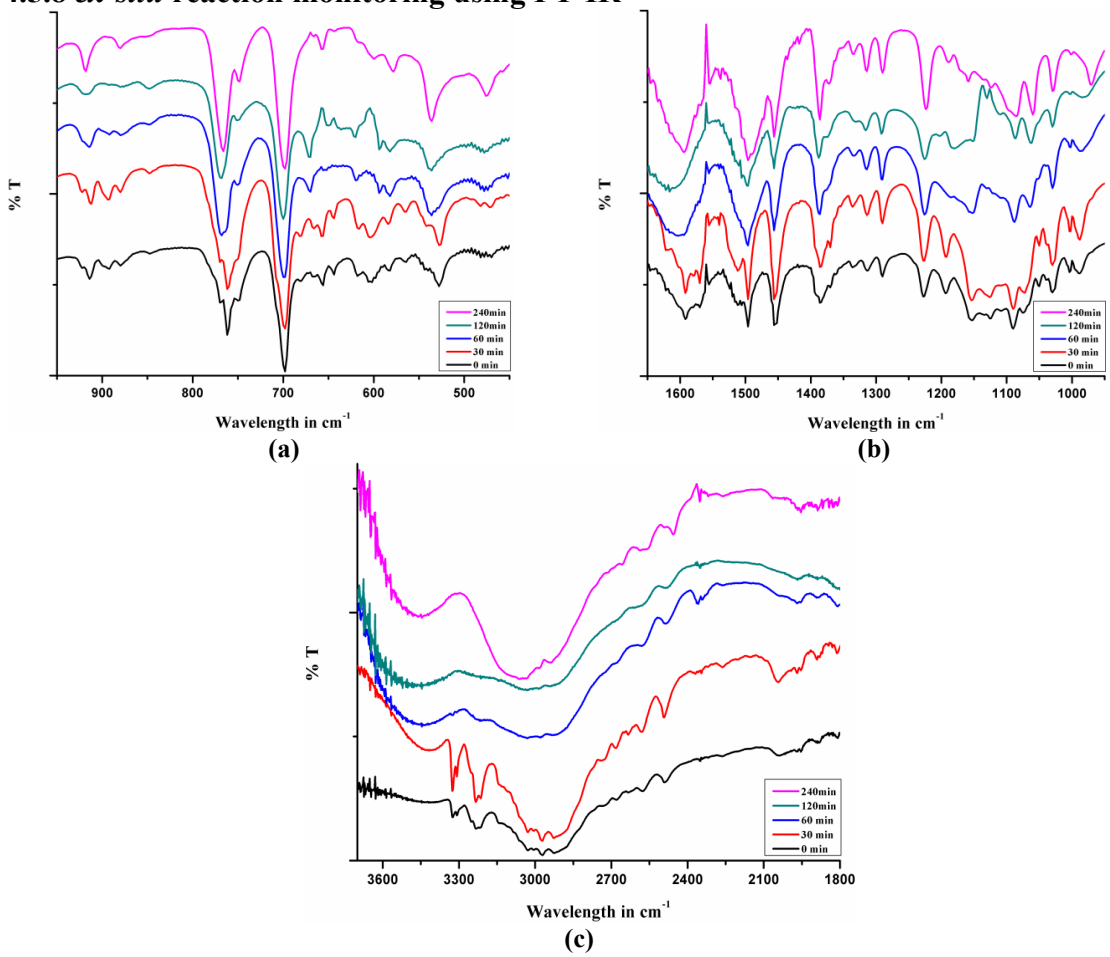

Fig. 4.21: (a-c) *ex-situ* FT-IR monitoring of $A_R/A_S \rightarrow B_R/B_S$ in KBr pellet

The FT-IR spectrum of A_R/A_S (Figure 4.21a-c) was recorded in solid state. The KBr pellet (3mg of A_R/A_S in 100mg KBr) of A_R/A_S were kept in HCl gas environment and FT-IR spectra were recorded with increase of exposure time.

After 30 min. almost all bands retain their position but color of pellet changes from green to green yellow. After one hour substantial change occurred and pellet becomes brown. IR spectra indicate the loss of $-NH_2$ symmetric and antisymmetric stretching vibration and formation of $-NH_3^+$ stretching vibration at 3028-3055cm^{-1}. Formation of weak band at 1622cm^{-1} indicates the $-NH_3^+$ symmetric bending mode. $-CH_3$ deformation mode became a sharp while $-CH_2$ rocking mode merged in single band and shifted slightly. Out of plane ring deformation modes get merged and became sharp. After 60 mins all bands become sharp in nature without further change up to 120 mins. After 240 mins A_R/A_S transforms to B_R/B_S. (Comparison with standard IR spectrum of B_R/B_S).

4.5.9 Powder XRD

4.5.8.1:

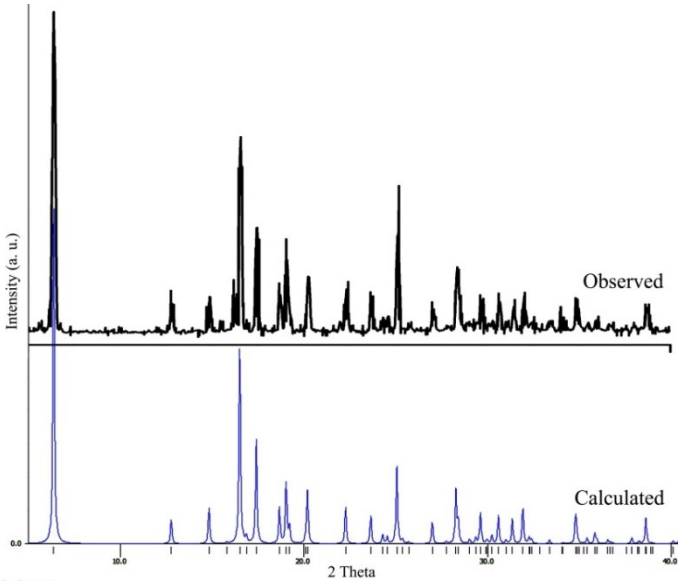

(a)

Fig. 4.22: **PXRD pattern of B_R obtained after keeping A_R during 150 minutes in the HCl gas environment after the solid-gas interface synthesis. Wavelength: 1.54056 Å.**

4.5.8.2 *ex-situ* reaction monitoring

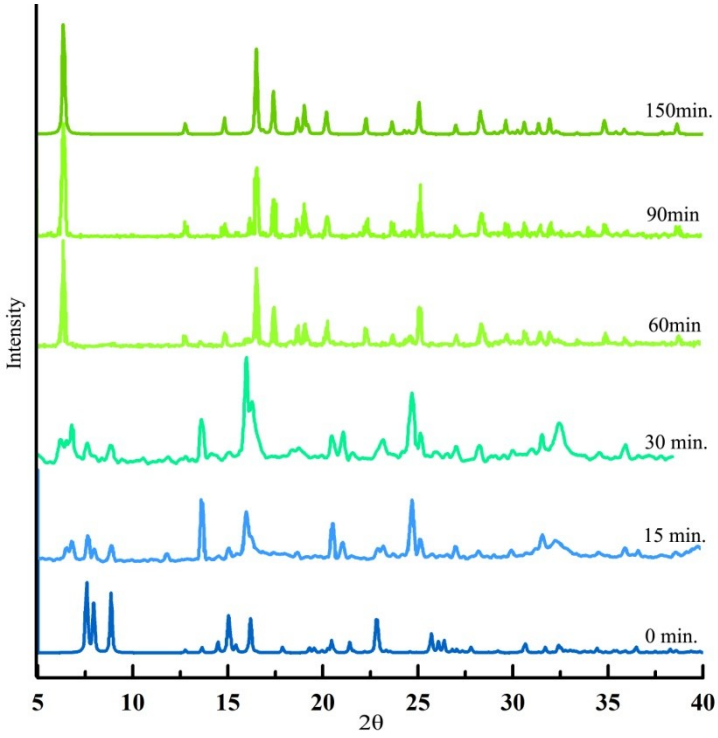

Fig. 4.23: PXRD time-dependent transformation of A_R to B_R in HCl gas environment measured at 298 K. Wavelength: 1.54056Å

4.5.8.3 $B_S \rightarrow A_S$ after KOH treatment

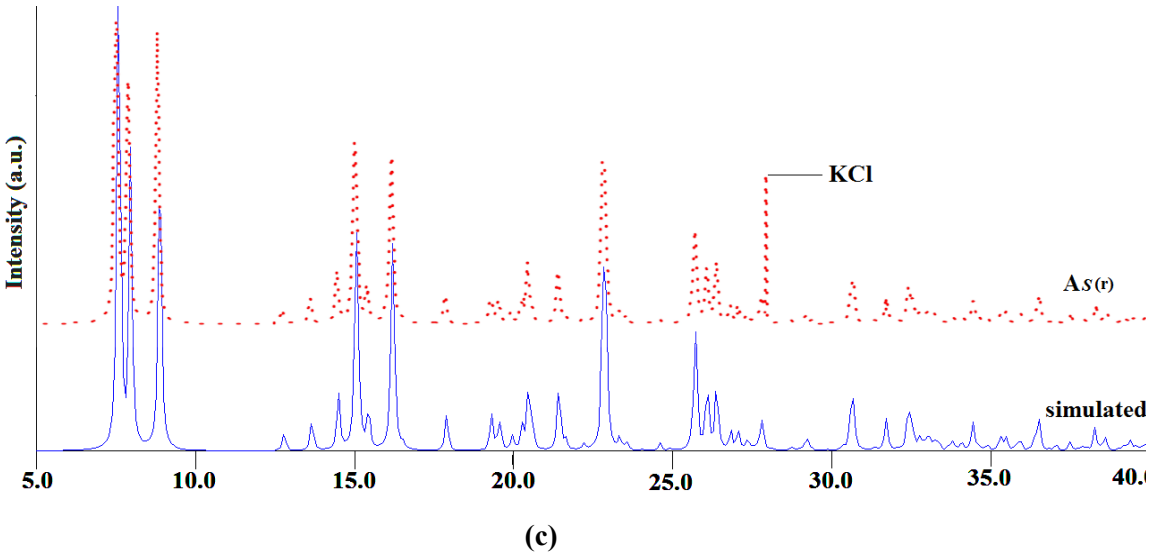

(c)

Fig. 4.24: XRPD of conversion of $B_S \rightarrow A_S$ (r) after KOH. (Note the peak due to eliminated KCl at 2θ=28°)

4.5.10 Solid state CD spectra

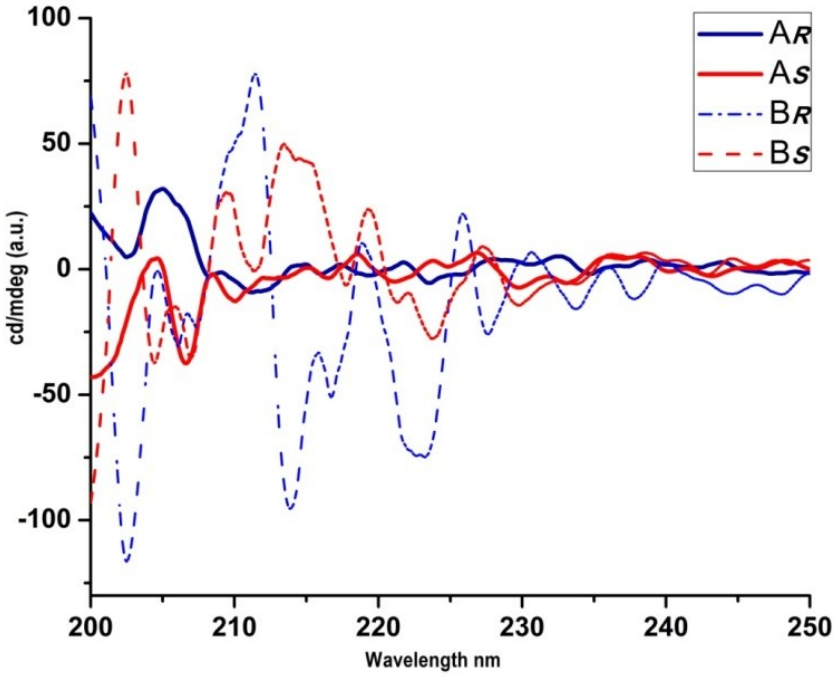

Fig. 4.25: Solid state CD spectra of A_R, A_S, B_R and B_S in nujol

A_R exhibits a negative dichroic signal at 204 nm and positive dichroic signal at 206 nm while A_S shows Cotton effect with opposite sign at the same wavelength (Figure 4.25).

$\mathbf{A}_{\boldsymbol{S}}$ exhibits a positive dichroic signal at 205 nm which shifted to blue region at 202 nm during the conversion along with the generation of new dichroic signals (Figure 4.26). After conversion, $\mathbf{B}_{\boldsymbol{R}}$ exhibits a negative dichroic signal at 203, 214 and 224 nm and a positive Cotton effect at 212 and 220 nm. $\mathbf{B}_{\boldsymbol{S}}$ shows Cotton effects of the opposite sign at the same wavelengths.

Grinding $\mathbf{B}_{\boldsymbol{S}}$ with KOH led to a color change from yellow green into bluish green in minutes (Figure4.26). No change in sign of cotton effect during conversion of $\mathbf{B}_{\boldsymbol{S}}$ to $\mathbf{A}_{\boldsymbol{S}}$ **(r)**.

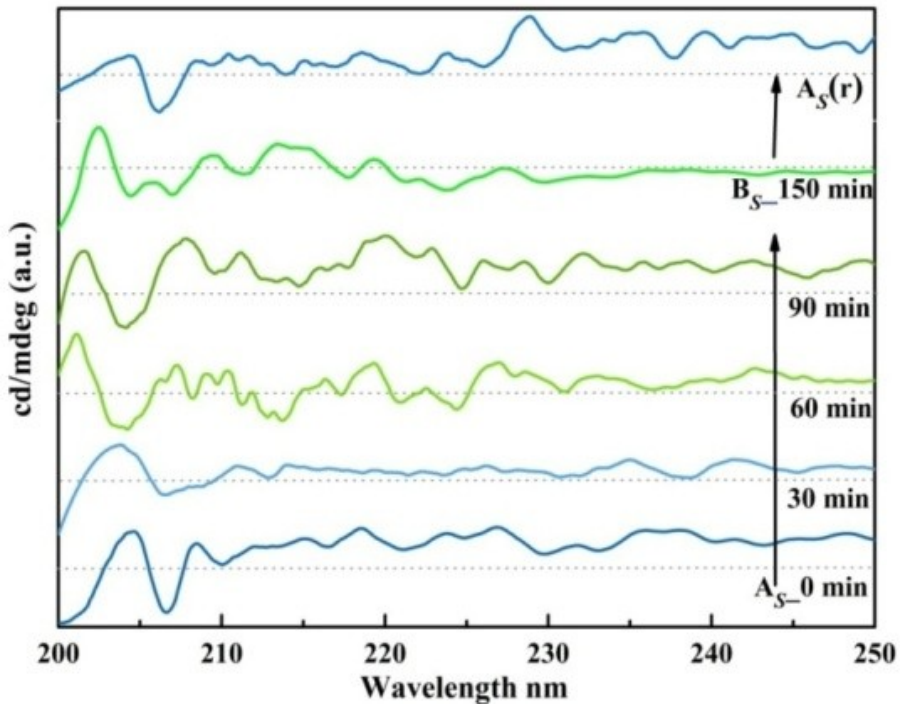

Fig. 4.26: Circular Dichroism study: Monitoring of HCl gas adsorption with time during transformation of A_1 to B_1 and desorption A_S (r). (colour of the spectra are matching with the colour of the sample during this transformation)

4.5.11 Specific Optical Rotation (SOR) activity on A_R and A_S, B_R and B_S

Table 4.6: SOR data on A_R and A_S, B_R and B_S in methanol at 30ºC

Sr. No.		Angle of minimum deviation (°)			Average (°)
1	$\mathbf{A_R}$	+40.8	+38.4	+37.6	+38.9º
2	$\mathbf{A_S}$	-33.8º	-33.0º	-38.4º	-35.1º
3	$\mathbf{B_R}$	-7.9º	-7.7º	-8.4º	-8.0º
4	$\mathbf{B_S}$	-7.2º	-7.7º	-8.6º	-7.9º

12.2 *ex-situ* reaction monitoring of conversion of A_S to B_S and $B_S \rightarrow A_S$ with time of exposure to HCl

Table 4.7: *ex-situ* reaction monitoring with time of conversion of A_S to B_S using SOR in methanol and S1(r) showed SOR of conversion of $B_S \rightarrow A_S$ at 30ºC

Sr. No.	$A_S \rightarrow B_S$ with time	Angle of minimum deviation (°)			Average (°)
1	0 min	-38.4º	-39.3	-38.4º	-38.4º
2	60 min	-7.1º	-7.3º	-7.6º	-7.4º
3	150 min	-8.2º	-7.7º	-8.5º	-8.1º
4	S1(r)*	-21.07	-21.09	-21.2	-21.1

* After KOH treatment.

$\mathbf{A_R}$ has a specific rotation of +38.4º while the other enantiomer $\mathbf{A_S}$ has a specific rotation of -38.4º at 30ºC(Table 4.6). $\mathbf{A_S}$ when exposed to HCl vapours changes to green coloured which showed specific rotation of -7.4º after 60 minutes (Table4.7). The reason behind decline in SOR value may be due to formation of ammonium cation of (*S*)-(−)-α-Methyl benzylamine ligand. After 150 min., $\mathbf{A_S}$ completely transformed to $\mathbf{B_S}$ with specific rotation of -8.1º which completely matches with the standard SOR activity (-7.9º) of $\mathbf{B_S}$. Grinding B_S with KOH results into bluish green powder from yellow green with SOR activity -21.1º. Decrease in SOR value may be due to presence of water along with methanol. This study suggests that during inter conversion of $A_S \rightarrow B_S$ and reversibly from $B_S \rightarrow A_S$ the absolute configuration of ligand remained same and no racemisation take place.

4.5.12 Theoretical study

A_S

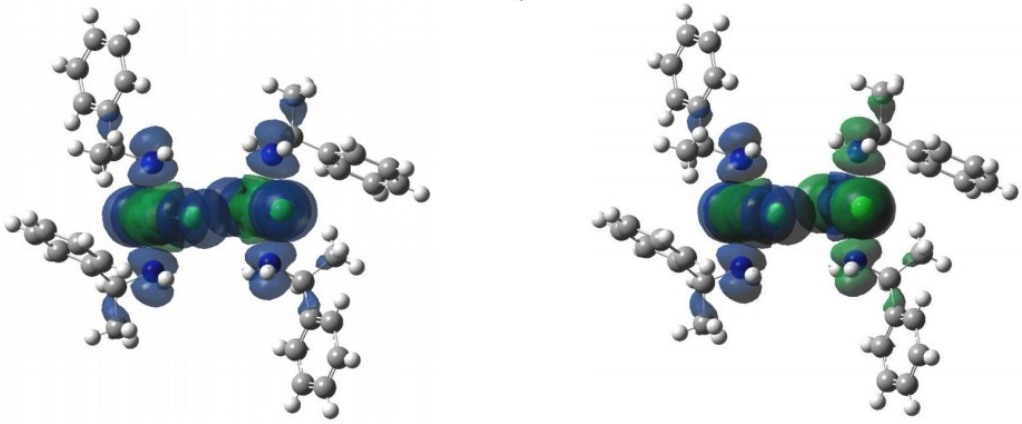

Triplet State
Spin density = 2.0

Singlet State
Spin density = 0.0

B_S

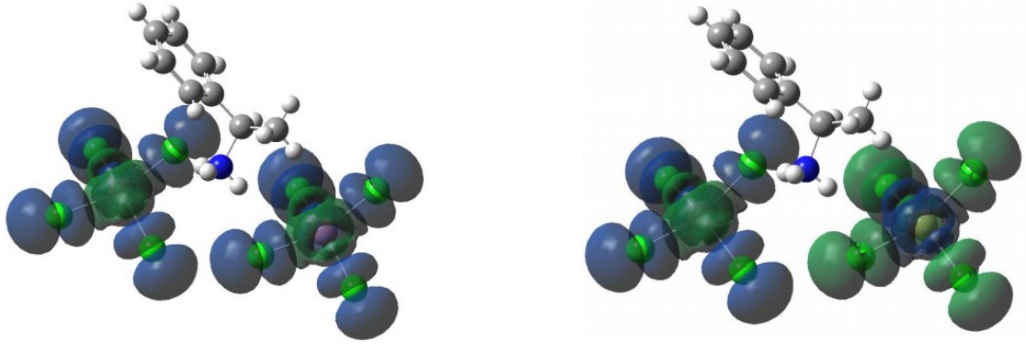

Triplet State
Spin density = 2.0

Singlet State
Spin density = 0.0

For both complexes ΔE = E(Singlet) – E(Triplet) ≈ 0

Fig. 4.27: Theoretical study on A_S and B_S

Theoretical study on s **A_S** (Figure 4.27a) and **B_S** (Figure 4.27b)were carried out using UB3LYP/6-31+G(d,p) method. LANL2DZ basis set for Cu atom. **A_S** showed that the spin density in triplet state resides mainly on Cu and Cl atoms, partially on the NH_2 groups while it is zero in singlet state. **B_S** shows the spin density in triplet state resides only on Cu and Cl atoms and not on the ligand while it is zero in singlet state.

4.5.13 Different structures of ligands

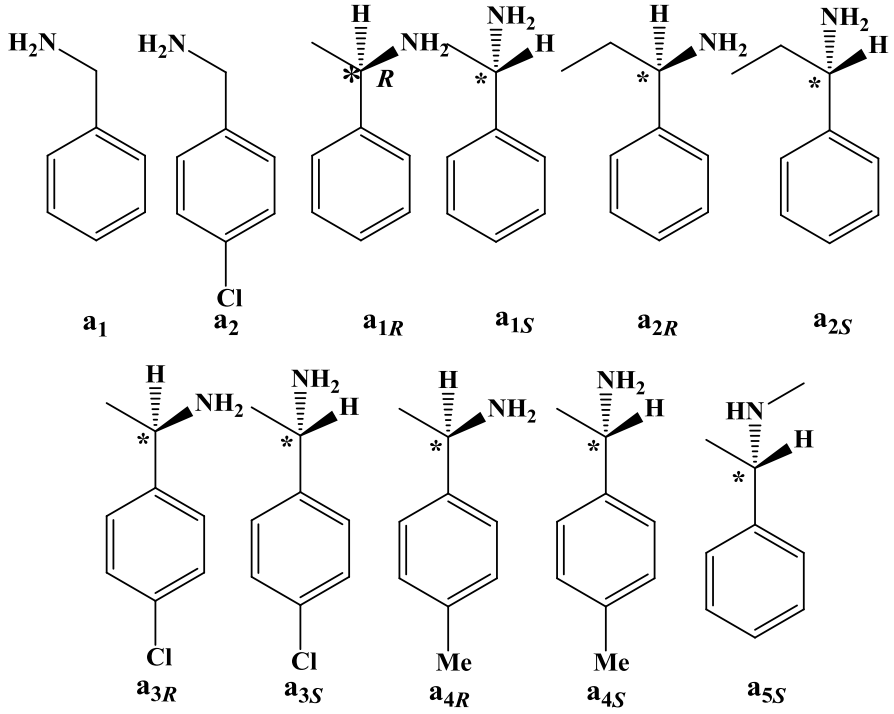

Fig. 4.28: Different structures of ligands employed during present investigation

4.6 Crystal to Crystal transformation at Solid-Gas interfaces: (Ideal Molecular Sensor)

After accommodation of HCl gas in molecular crystal, we observed very clear changes in optical properties, $\mathbf{A_1}$ to $\mathbf{B_1}$ systems. Recently, we [5b] and other [15] have shown that **B**-type structures, A_2CuCl_4, not only show interesting molecular magnetic properties but also exhibit multiferroic behavior. The present set of compounds is no exception, and shows distinct changes in magnetic (Section 4.6.1; Figure 4.29), thermochromic (Section 4.6.2; Figure 4.30 and Section 4.6.3; Figure 4.31) as well as ferroelectric behavior (Section 4.6.4; Figure 4.32).

Thus, these studies also provide novel candidates for molecularly driven multiferroic [16] and/or multifunctional compounds [17]. Detailed studies of this behavior are underway.

4.6.1 Solid state EPR

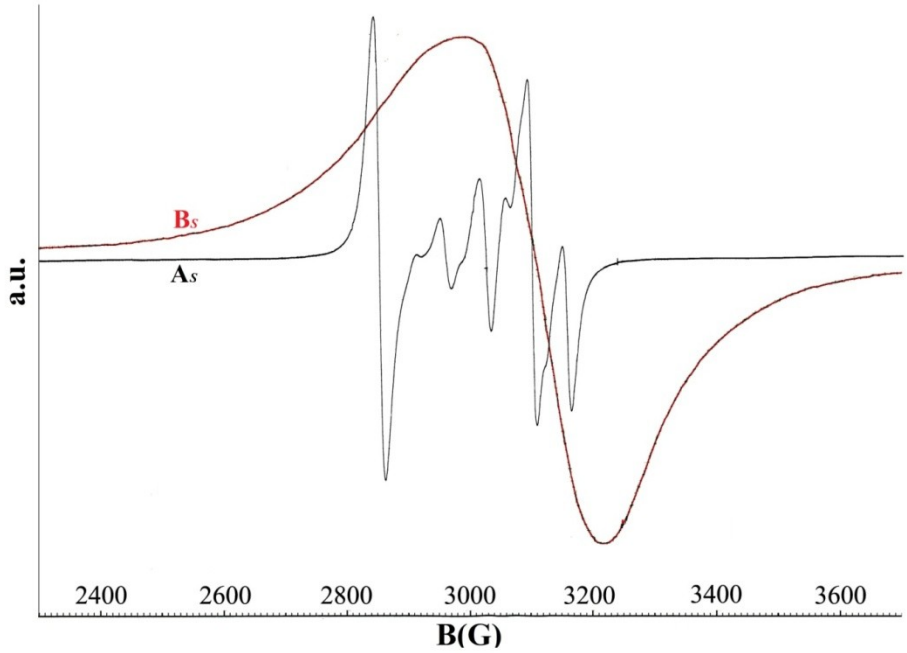

Fig. 4.29: Solid state EPR spectra of A_S and B_S at room temperature

A_S: g||= 2.14; $g_{\perp}$ = 2.13; $g_{avg.}$= 2.13

B_S: g||= 2.16; $g_{\perp}$ = 2.08; gavg.= 2.13

4.6.2 DSC and Thermochromism behavior for B_1

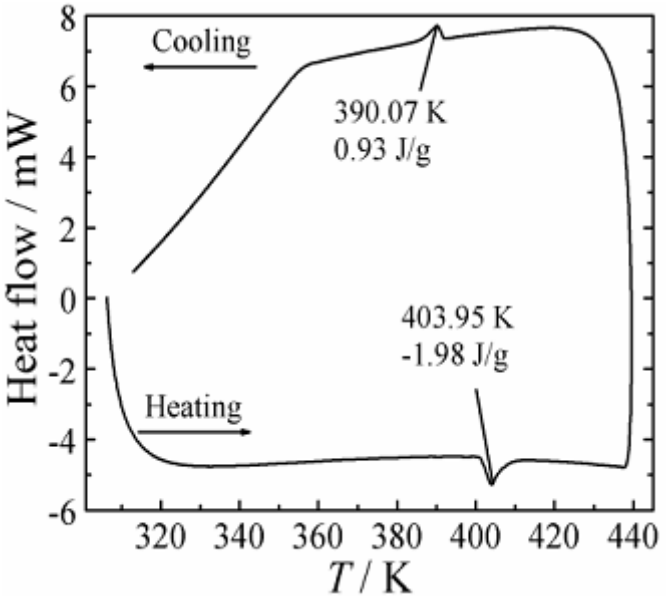

(a)

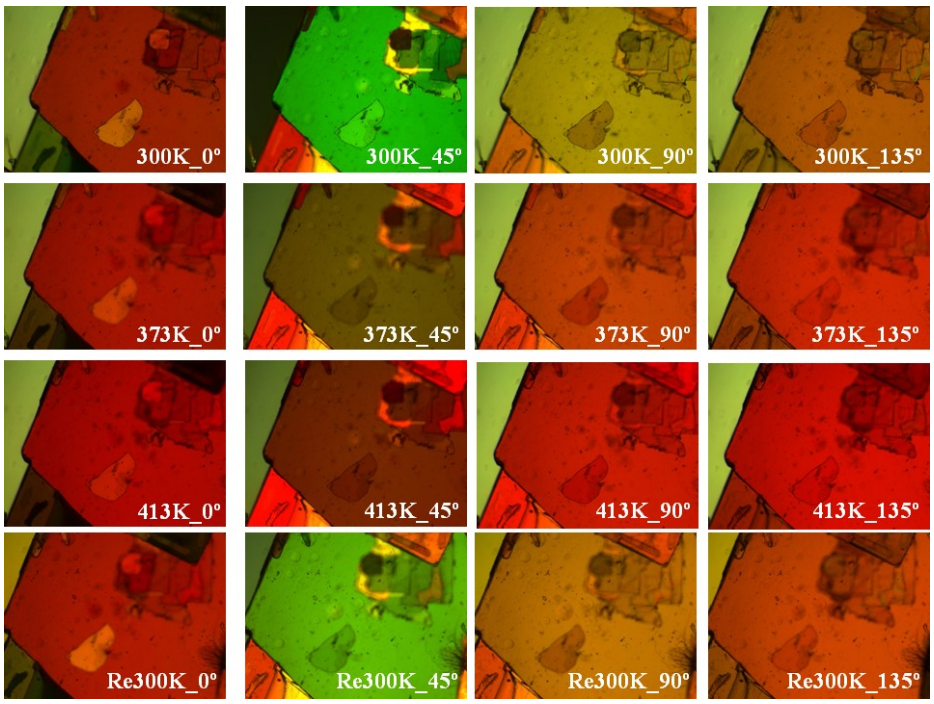

(b)

Fig. 4.30: (a) DSC and (b) Thermochromic behavior for B_1 using polarizing microscope

4.6.3 DSC and Thermochromic behavior for B_R / B_S

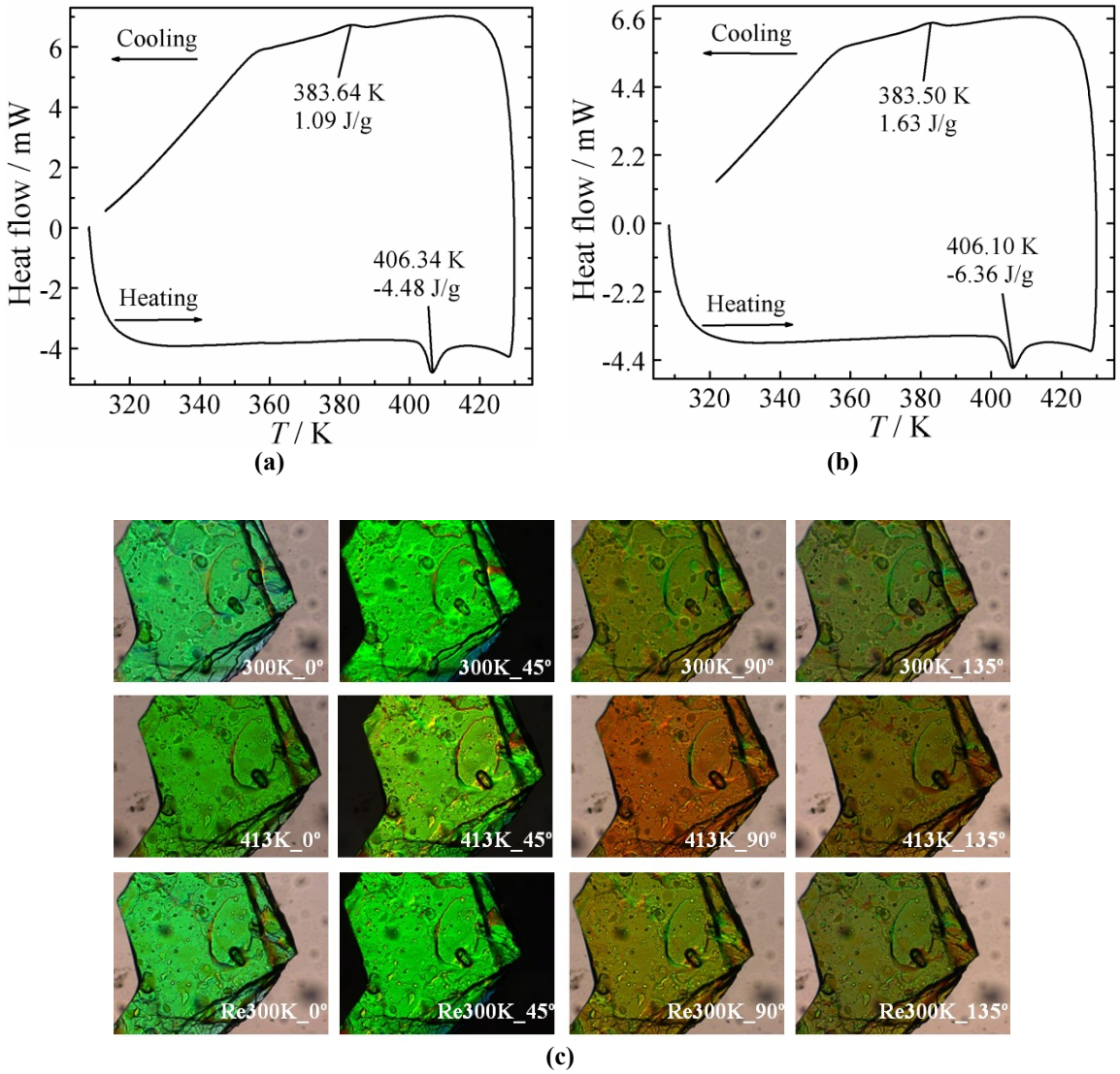

Fig. 4.31: (a) DSC of B_R, (b) DSC of B_S and (c) Thermochromic behavior for B_R / B_S using polarizing microscope

To confirm different degradation pathways and exothermic behavior of DTA, we carried out DSC on all complexes and their complexes from 298K to their degradation temperature. DSC studies on complexes shows presence of reversible solid-solid phase transition and non solvated as thermogram showed a single thermally induced endothermic transition. These solid-solid phase transitions are related to the thermochromic behavior as color of complexes changes with temperature.

Table 4.8: DSC chart of compound B_1, B_R and B_S at different temperatures

Compounds	Phase Transition (300K-450K)			
	Heating		Cooling	
	Temperature [K]	Enthalpy[Jg^{-1}]	Temperature [K]	Enthalpy[Jg^{-1}]
B_1	403.95	-1.98	390.07	0.93
B_R	406.10	-6.36	383.50	1.63
B_S	406.34	-4.48	383.64	1.09
	Phase Transition (160K-300K)			
B_1	No transition observed.			
B_R	No transition observed.			
B_S	No transition observed.			

The thermodynamic values obtained for the endothermic thermochromic phase transition during heating are 403.95K (-1.98 Jg^{-1}) for compound $\mathbf{B_1}$, 406.10K **(**-6.36Jg^{-1}**)** for $\mathbf{B_R}$ and 406.34K (-4.48Jg^{-1}) for $\mathbf{B_S}$. During cooling, all compounds show the single exothermic peak at 390.07K (0.93Jg^{-1}) for $\mathbf{B_1}$, 383.50K 1.63Jg^{-1}**)** for $\mathbf{B_R}$ and 383.64K 1.09Jg^{-1}) for $\mathbf{B_S}$. Thermodynamic data for these thermochromic complexes are shown in Table 4.8.

To confirm these phase transition compounds were analyzed using polarizing microscope. The polarizing microscope images show that at phase transition temperature the compounds show the thermochromic behavior. The compound $\mathbf{B_1}$ showed reversible color change from Yellowish Orange ↔ Red, compound $\mathbf{B_R}$ and $\mathbf{B_S}$ showed color change from Green Yellow ↔ Yellow Brown color confirms thermochromic nature. These solid-solid transitions are reversible in nature and can be repeated many cycles without any observable change in peak position.

The yellowish orange color corresponds to the Cl-Cu-Cl *trans* angle (138.70º and 145. 17º) as these angles due to distorted tetrahedral geometry of $CuCl_4^{2-}$ anion. The green-yellow color of $\mathbf{B_R}$/$\mathbf{B_S}$ due to Cl-Cu-Cl *trans* angle (153.9º) corresponds to the tetrahedral geometry which having angles in between square planar and tetrahedral structure. Thermochromism observed due to change in these angles hence if color changes to Red or Brown, the angle become less and the structure will be in more distorted tetrahedral structure [18].

An intriguing feature of many copper (II) chloride complexes is their thermochromic behavior in the solid state. The phase transition observed in the DSC can also be detected by the color change of the sample i. e. thermochromism. This can be observed by the polarizing microscope (POM) equipped with a cooling and heating stage. When heated about to phase transition temperature the compound $\mathbf{B_1}$ (Figure 4.30b: 300K_90º↔413K_90º) showed reversible color change from Yellowish Orange ↔ Red (403.95K) while compound $\mathbf{B_R}$ and $\mathbf{B_S}$ (Figure 4.31b: 300K_90º↔413K_90º) showed color change from Green Yellow ↔ Yellow Brown (406K) color confirms thermochromic nature.

4.6.4 PE Loop measurement

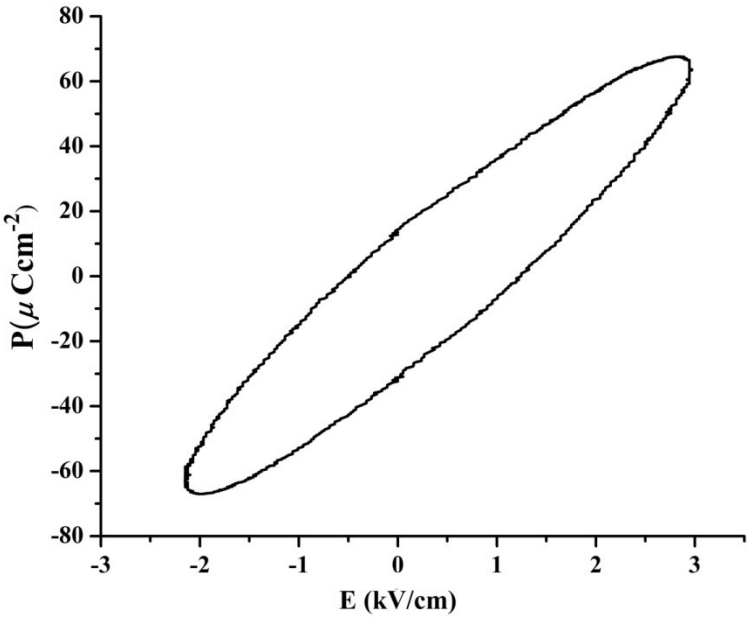

Fig. 4.32: PE Loop measurement of B_R

A ferroelectricity loop measurements was performed on $\mathbf{B_R}$ in pellet form. At 300 K, we observed large spontaneous polarization, switchable with a relatively small electric field at room temperature. The ferroelectricity loop measurements (PE loop) on $\mathbf{B_R}$ is depicted in Figure 4.32.

Hysteresis measurements gave a well-defined loop for $\mathbf{B_R}$ with the maximum field of 0.865kVcm^{-1}. The coercive field Ec observed at 0.865 kVcm^{-1} while remnant polarization *P*r observed at 155.10 μCcm^{-2} at 300 K.

4.7 Reversible Crystal to Crystal transformation at Solid-Liquid interfaces: (Molecular Nature due to Self assembly, Molecular Recognition and Anchimeric assistance)

These non-porous adsorptive compounds, $\mathbf{A}_{\boldsymbol{R}}/\mathbf{A}_{\boldsymbol{S}}$, selectively accommodate supramolecularly arranged azide ligand [19] with the help of molecular recognition (Section 4.7.1; Scheme 4.5) and colour change from blue to dark green, as shown in Section 4.7.1.1; Figure 4.34 and in Figure 4.1.

This transformation is totally different than that is observed at solid-gas interface because azide anion is incorporated with the help of self-assembly of auxiliary ligand. To the best of our knowledge, this is a first example, where true 'molecular nature' is reflected owing to cyclic reversible nature of $\mathbf{C}_{\boldsymbol{R}}$ to $\mathbf{B}_{\boldsymbol{R}}$ and $\mathbf{A}_{\boldsymbol{R}}$ to $\mathbf{B}_{\boldsymbol{R}}$ and further shows this transformation happens with retention of single crystalline character.

$\mathbf{C}_{\boldsymbol{R}}/\mathbf{C}_{\boldsymbol{S}}$ crystallized into the $P2_12_12_1$ acentric space group [20]. Here Cu (II) ions are in three crystallographically different environments, two square pyramidal in which each Cu(II) is coordinated with five end-on (*EO*) azide bridges, and one square planar coordinated with nitrogens of two amine ligands and two end-to-end (*EE*) azide bridges (Section 4.7.3; Figure 4.36a&b). Self-assembly forms neutral 2D brick-wall layers with a repeating azido-bridged eight membered copper brick (Section 4.7.3; Figure 4.36-c&d).

These $\mathbf{C}_{\boldsymbol{R}}$ and $\mathbf{C}_{\boldsymbol{S}}$ compounds have been reported and shown multifunctional properties which include ferromagnetic and weak ferroelectric behavior. That means azide accommodation can be easily detected by various techniques at solid-liquid interface.

This transformation is driven by 'self-assembly' of an auxiliary ligand because chemisorption of azide anion happens with its loss, as shown using following reaction,

$$3\ ((R)\text{-}(+)C_6H_5CH(CH_3)NH_2)_2CuCl_2 + 6\ NaN_3 \longrightarrow [Cu_3((R)\text{-}(+)C_6H_5CH(CH_3)NH_2)_2(N_3)_6]_n + 6\ NaCl + 4\ (R)\text{-}(+)C_6H_5CH(CH_3)NH_2$$

But, in-spite of this ligand loss, true molecular nature of this reaction is remained intact due to cyclic reversible transformations from **C** to **B** and **B** to **A** as shown in Figure 4.1 (Section 4.7.3; Scheme 4.6 & 4.7).

This means, $\mathbf{C}_{\boldsymbol{R}}/\mathbf{C}_{\boldsymbol{S}}$ when exposed to dry HCl vapors forms double salt $\mathbf{B}_{\boldsymbol{R}}/\mathbf{B}_{\boldsymbol{S}}$, which in turn can desorb HCl to give back $\mathbf{A}_{\boldsymbol{R}}/\mathbf{A}_{\boldsymbol{S}}$, thus confirming molecularity of the overall reaction (Section 4.7.4.2; Figure 4.38).

Molecular recognition of this transformation is reflected due to its selective sorption of azide anion, (this is observed mainly for A to C transformation and not for B to C transformation) in spite of presence of other anions, such as Cl^-,Br^-, NO_3^-, and SCN^- (Section 4.7.5). In-spite of this, the solid state CD spectra on the single crystals revealed that this transformation happens with retention of chirality(Section4.7.6;Figure4.39-4.40). The reason for the observed Single crystal to single transformation (SCSC) transformation resides in two factors (a) Lattice energy of NaCl crystal might drive reaction 1; (b) Self-assembly can help in directing movement of auxiliary ligand. We associate this SCSC or fast crystallization to anchimeric assistance. In organic chemistry, anchimeric assistance is observed when neighboring atoms/molecule facilitates the activity at the reaction center. Normally, the ratesof anchimeric assisted reactions are very fast, and happen without racemization.[21]To support these views, interestingly, weobserved novel path of 'molecular' interactions at solid-liquid interface by auxiliary ligands. Auxiliary ligand in **A'**is *p*-chloro methyl benzylamine and **A**is methyl benzylamine. Figure 4.33 shows crystal to crystal transformation of **A'**(A' exists as polycrystalline) to 1-dimentional helical chain structure **C'**and **A** to 2-dimensional **C**with SCSC transformation.[22]This means auxiliary ligands self-association help in molecular recognition of azide anion and hence crystallization. The fast rate of crystallization is required to maintain observed SCSC transformation, and hence anchimeric assistance. Therefore study on the rate of crystallization or SCSC of present reactions will certainly open up a new view for understanding anchimeric assistance along with self-assembly and molecular recognition process in coordination compounds.

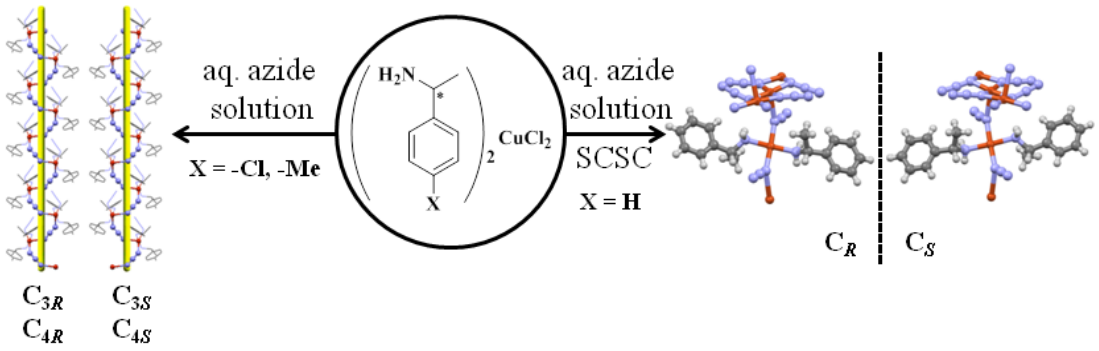

Fig. 4.33. Role of molecules during self-assembly and molecular recognition, a true anchimeric assistance during crystal to crystal transformation from A to C

This report displays non-porous compounds ‘molecular’ expressive ability in the form of self-dissociation, molecular recognition, self-assembly and more importantly first time anchimeric assistance by maintaining crystalline state. Thus, molecular pathways can act as flexible host to ‘accommodate’ guest molecules from gas as well as liquid state with distinct measurable change in optical, magnetic, thermochromic, and ferroelectric properties will surely help in generating novel molecular sensors.

4.7.1 Transformation of compounds:

Scheme 4.5: Transformation of C_R/C_S from A_R/A_S (Single crystal to single crystal transformation)

$$(R\text{-}NH_2)_2CuCl_2 + NaN_3 \xrightarrow[\text{Solid-liquid interface}]{\text{Water}} [Cu(R\text{-}NH_2)_2(N_3)_6]_n \quad \textbf{(C)}$$

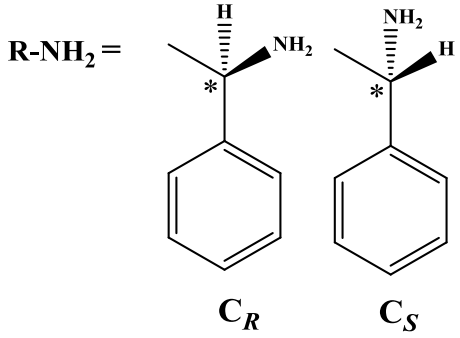

Scheme 4.6: Transformation of C_R/C_S from B_R/B_S

$$(R\text{-}NH_3)_2CuCl_4 \xrightarrow[\text{Solid-liquid interface}]{\text{Aq. azide sol.}} [Cu(R\text{-}NH_2)_2(N_3)_6]_n \quad \textbf{(C)}$$

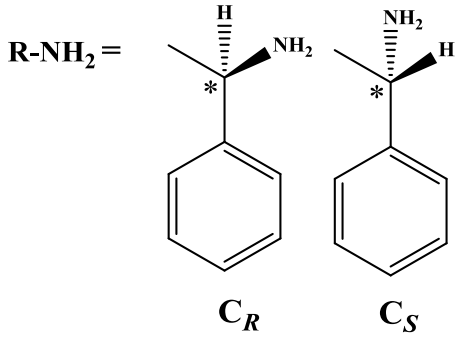

4.7.1.1 Transformation of $B_1/B_R/B_S$ from A_1.

Crystals of B_R/B_S filter paper dipped in a watch glass containing saturated aqueous solution of sodium azide (1M) for 5 seconds. The color of the B_R/B_S changes from yellow green to dark green giving powder sample of C_R/C_S.

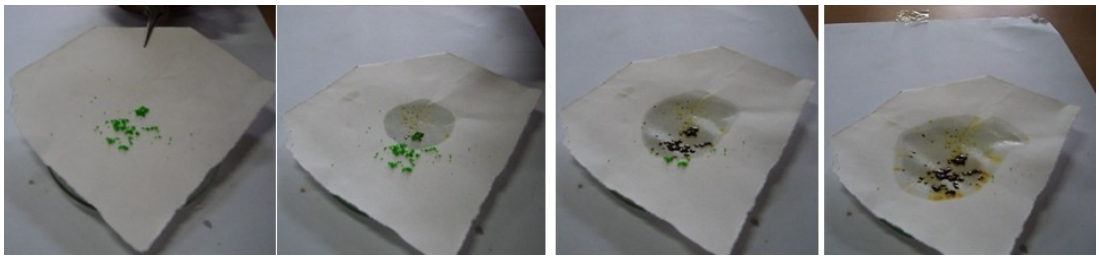

(a) (b) (c) (d)

Fig. 4.34: Crystal transformation of $B_R/B_S \rightarrow C_R/C_S$

Scheme 4.7:Transformation of B_R/B_S from C_R/C_S

$$[Cu(R\text{-}NH_2)_2(N_3)_6]_n \xrightarrow[\text{Solid-gas interface}]{\text{Conc.HCl vapours}} (R\text{-}NH_3)_2CuCl_4 \quad (B)$$

R-NH_3 =

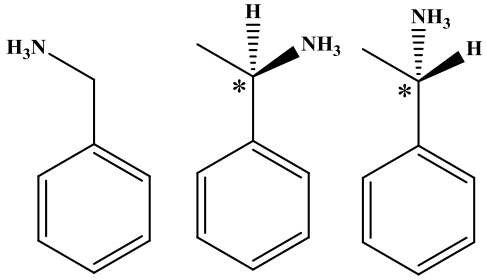

B_1 B_R B_S

4.7.1.2 Transformation of B_R/B_S from C_R/C_S

Sample vial containing crystals of C_R/C_S (1 g) was kept in HCl gas chamber. The reaction took place over a 10-12 hrs to form B_R/B_S with observable color change from dark green to yellow green.

Fig. 4.35: Crystal transformation of $C_R/C_S \rightarrow B_R/B_S$

4.7.1.3 Transformation of C_R/C_S from A_R/A_S

Crystals of A_R/A_S on filter paper dipped in a watch glass containing saturated aqueous solution of sodium azide (1M) for 5 seconds. The color of the A_R/A_S changes from blue to green giving crystals of C_R/C_S.

Compound C_R FT-IR (KBr): 3350 (m), 3317 (s), 3298(w), 3237(s), 3210 (s), 3138 (s), 3083(w), 3028 (m), 3006 (w), 2965 (s), 2921 (w), 2867 (w), 2077 (ssh), 2040 (ssh), 1588 (s), 1573 (vs), 1493 (m), 1453 (vs), 1388 (s), 1374 (s), 1341 (s), 1306 (m), 1287 (m), 1240 (s), 1221 (s), 1150 (vssh), 1089 (vssh), 1074 (vs), 1064 (vs), 1043 (s), 1024 (s), 1003 (s), 994 (s), 926 (w), 910 (m), 888 (s), 782 (m), 757 (vs), 708 (s), 698 (ssh), 670 (vs), 603 (s), 561 (m), 543 (m), 529 (w), 474 (w) and 441 (w) cm^{-1}.

Compound C_S FT-IR (KBr):3351 (m), 3315 (s), 3295(w), 3232(s), 3212 (s), 3138 (s), 3058(m), 3029 (m), 2961 (s), 2924 (w), 2075 (ssh), 2042 (ssh), 1586 (s), 1571 (vs), 1491 (m), 1456 (vs), 1387 (s), 1371 (s), 1342 (s), 1308 (m), 1290 (m), 1237 (s), 1218 (s), 1191 (w), 1148 (vssh), 1091 (vssh), 1071 (vs), 1067 (vs), 1042 (s), 1021 (s), 1003 (s), 994 (s), 926 (w), 910 (m), 900 (w), 888 (s), 848 (w), 782 (m), 769 (w), 757 (vs), 710(s), 695 (ssh), 672 (vs), 602 (s), 561 (m), 542 (m), 530 (w), 473 (w) and 442 (w) cm^{-1}.

4.7.2 Elemental analyses:

The calculated elemental analyses were consistent with the observed formulae of azide complexes.

Compound C_R: Anal. Calc. for $C_{16}H_{22}N_{20}Cu_3$: C, 28.05; H, 3.24; N, 40.89%. **Found:** C, 27.80; H, 3.30; N, 40.65%.

Compound C_S: Anal. Calc. for $C_{16}H_{22}N_{20}Cu_3$: C, 28.05; H, 3.24; N, 40.89%. **Found:** C, 27.85; H, 3.38; N, 40.59%.

4.7.3 Single Crystal X-ray Diffraction

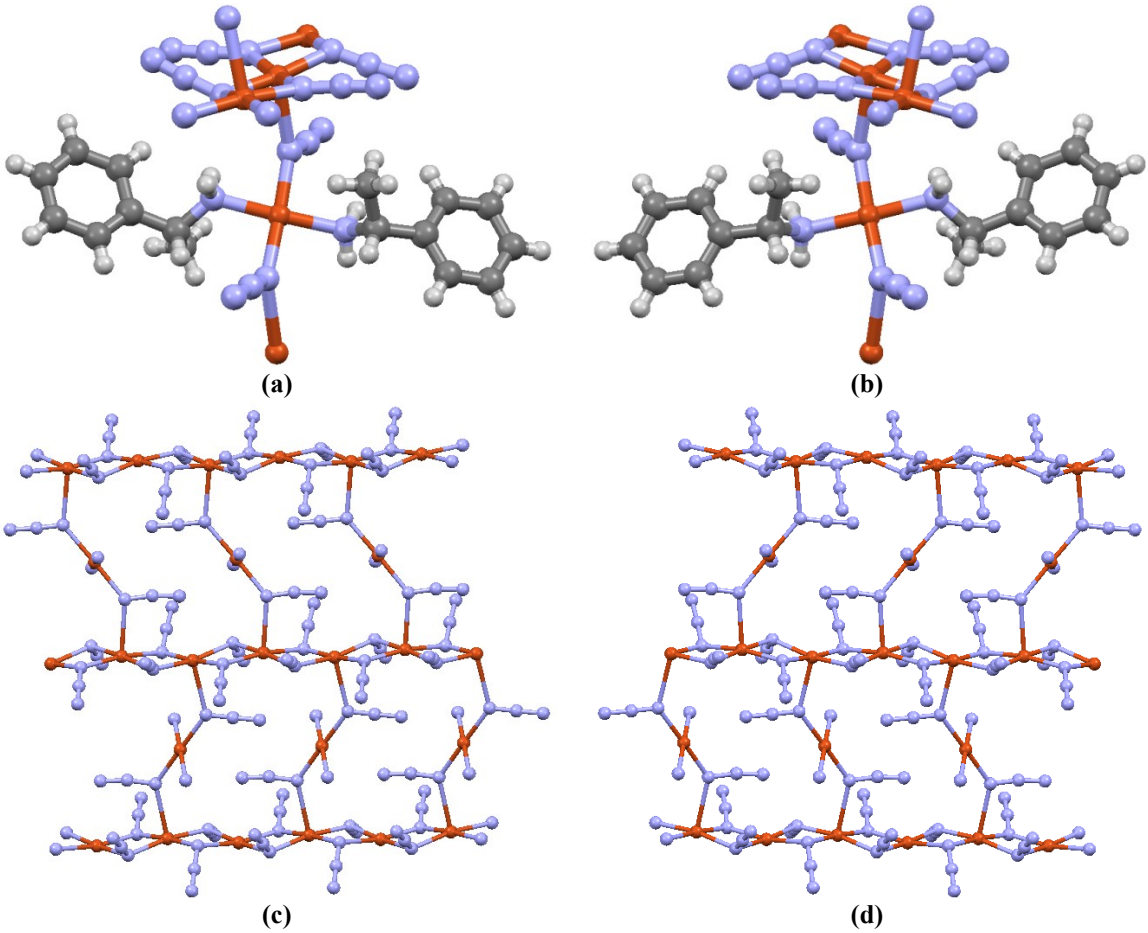

Fig. 4.36: Molecular view of (a) C_R and (b) C_S; Arrangement of the 2D brick-wall network (c) C_R and (d) C_S (H and C atoms of the amine ligands are omitted for clarity)

4.7.4 Powder X-ray diffraction:

The hydrogen-bonded salt arrays have been formed through coordination networks (compound $\mathbf{C}_{R}/\mathbf{C}_{S}$) by reverse reaction upon exposure of HCl (solid-gas interface) gas, found consistent with the salts (compound $\mathbf{B}_{R}/\mathbf{B}_{S}$) which are clearly revealed by X-ray powder diffraction study.

4.7.4.1 Comparison of observed XRPD pattern of bulk sample and simulated XRPD pattern (from single crystal data)

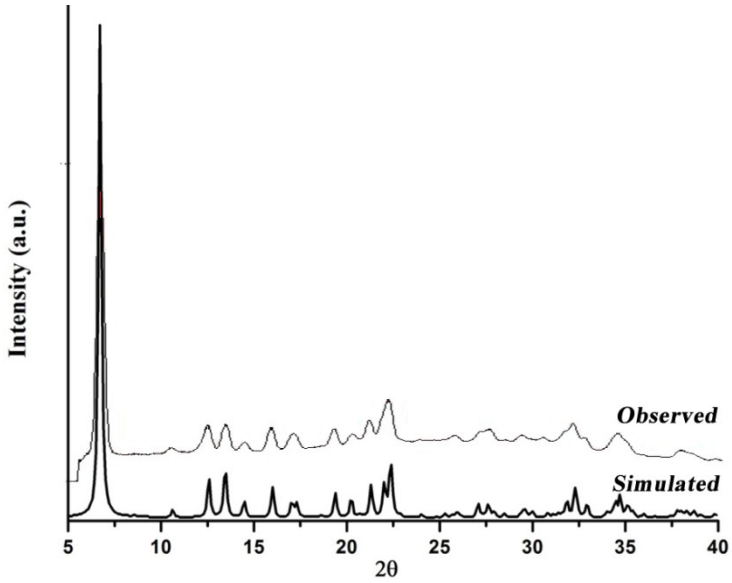

Fig. 4.37: Observed and simulated XRPD pattern of C_R

4.7.4.2 Comparison of observed XRPD pattern of bulk sample and simulated XRPD pattern (from single crystal data)

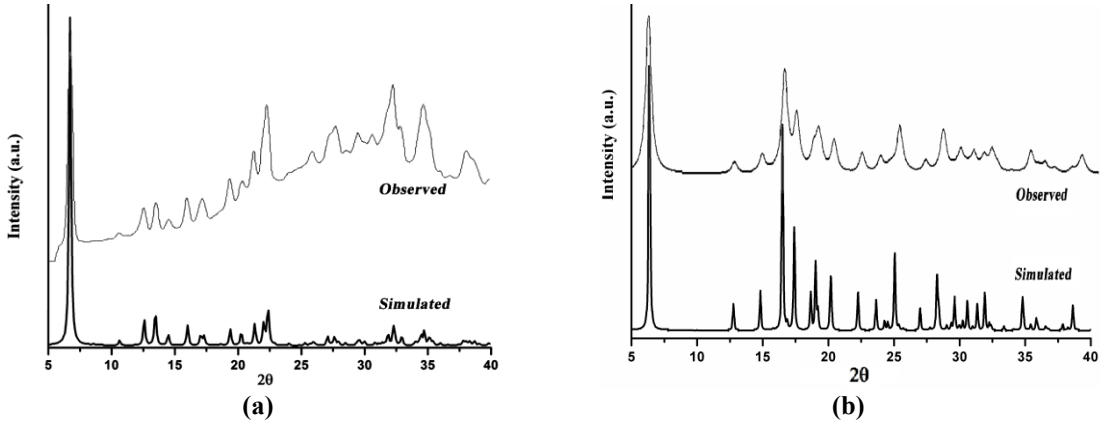

Fig. 4.38: (a) Observed and simulated XRPD pattern of C_R; (b) Observed and simulated XRPD pattern of B_R

The obtained patterns confirm that the simulated (single crystal) and bulk material properties are similar and it also confirms the phase purity of the bulk sample(Figure4.37) It is evident from the broad diffraction peaks in fig 4.38a that the samples prepared by the Solid-Liquid interface route have moderate crystallinity. This process is accompanied by a color change from yellow green to dark green. A good fit was obtained for the positions of the main reflections, but discrepancies in the intensities remain. These discrepancies might result from preferred crystallite orientation and anisotropic particle broadening.

Thus, exposure of a crystalline powder sample of the coordination network $\mathbf{C}_{\boldsymbol{R}}/\mathbf{C}_{\boldsymbol{S}}$ to HCl vapor (in a sealed vessel) led to the formation of microcrystalline yellowish green salt.

4.7.5 Anion Selectivity

Azide anion Selectivity of ((*R/S*)-(+/-)$C_6H_5CH(CH_3)NH_2)_2CuCl_2$ ($\mathbf{A}_{\boldsymbol{R}}/\mathbf{A}_{\boldsymbol{S}}$) from a mixture of Cl–,Br–, NO3−, SCN– and N_3– anions.

Blue color crystals of compound $\mathbf{A}_{\boldsymbol{R}}/\mathbf{A}_{\boldsymbol{S}}$ come contact with solution of mixture of salts contains different types of anions; these immediately turn into green color without dissolution. These anions can be differentiated into three groups (i) bridged (ii) halides (iii) *pseudo* halides.

0.3 g of compound $\mathbf{A}_{\boldsymbol{R}}/\mathbf{A}_{\boldsymbol{S}}$ was dipped in the 50 mL aqueous solution that dissolves NaN_3 (1 M), NaCl (1M), $NaNO_3$(1M), NaSCN (1M), NaBr (1M) for a period of 1-2 minutes.

The "transformed crystals" were then filtered and washed with water to remove any crystal-surface adsorbed salts. The selective azide exchange in the transformed crystals was confirmed by its infrared spectrum (Figure 4.24), X-ray powder pattern (Figure 4.28) and single crystal X-ray diffraction (Figure 4.27) that are identical to those of reported compound $[Cu_3((R/S)\text{-mba})_2(N_3)_6]_n$.

After transformation the solution was measured for its optical activity. The *R* isomer showed specific rotation $[\alpha]_D$ = –30, c = 0.1 g/mL in water-methanol while *S* isomer showed $[\alpha]_D$ = –30, c = 0.1 g/mL in water-methanol. The specific optical rotation measured for (*S*)-(-)-*α*-methylbenzylamine at 22°C is –40.3°.

Hence the present system (solid crystals of compound $\mathbf{A}_{\boldsymbol{R}}/\mathbf{A}_{\boldsymbol{S}}$) identifies an azide ion selectively from an aqueous solution consisting of a quantitative mixture of other common water soluble anions like Cl, Br, NO_3, SCN and N_3 etc.

4.7.6 Solid CD spectra

4.7.6.1 Solid CD spectra of A_R, A_S, C_R and C_S

The circular dichroism (CD) spectra measured in nujol confirm the enantiomeric nature of the SCSC transformed optically active complexes $\mathbf{C_R}$ and $\mathbf{C_S}$ (Figure 4.39 b).

The chiral nature of the enantiomorphs $\mathbf{C_R}$ and $\mathbf{C_S}$ was established by solid-state CD spectra of the same single crystal that was solved as single crystal XRD. Hence, the absolute chirality of the transformed compound $\mathbf{C_R}$/$\mathbf{C_S}$ established by single crystal X–ray studies are also complemented by the CD data.

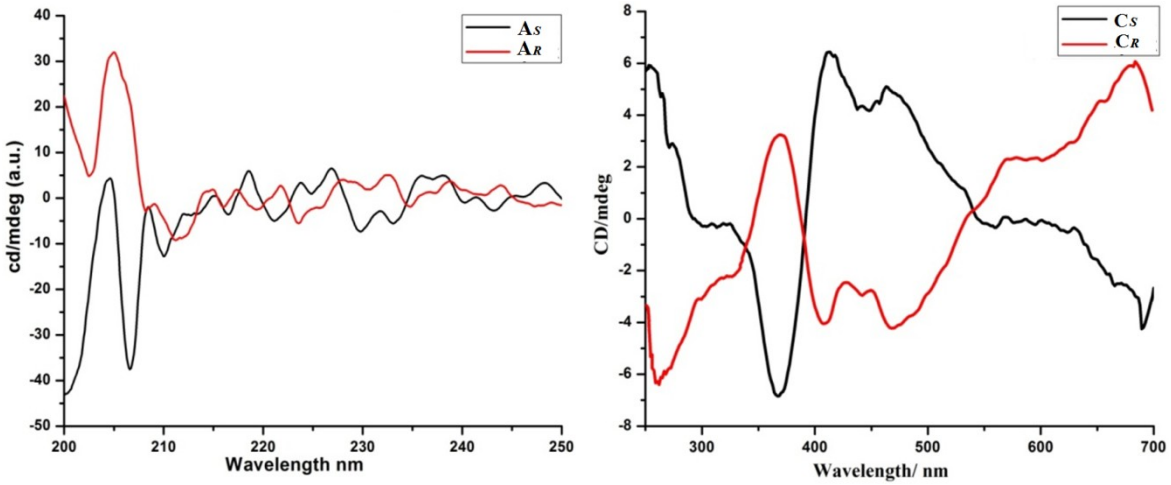

(a) (b)

Fig. 4.39: Solid state CD spectra in nujol (a) A_R and A_S ; (b) C_R and C_S

Compound $\mathbf{C_R}$ (*R*-isomer) showed positive Cotton effect around 365 nm and a negative cotton effect around 405nm and 460 nm, while $\mathbf{C_S}$ (*S*-isomer) shows Cotton effects of the opposite sign at the same wavelengths**.**

CD spectroscopy confirms no change in sign of cotton effect during conversion of $\mathbf{A_S}$ to $\mathbf{C_S}$ i.e. *S*-isomer making it stereochemically unaltered bond breaking and bond formation. Hence it is important that chiral information has been transferred fully in this SCSC transformation.

4.7.6.2 Solid CD spectra of B_R, B_S, C_R and C_S

The circular dichroism (CD) spectra measured in nujol confirm the enantiomeric nature of the reversibly transformed optically active compounds $\mathbf{B}_R$ and $\mathbf{B}_S$ to $\mathbf{C}_R$ and $\mathbf{C}_S$ respectively (Figure 4.40- a, b).

Compound $\mathbf{B}_R$ (*R*) exhibits a negative dichroic signal at 203, 214 and 224 nm and a positive Cotton effect at 212 and 220 nm while compound $\mathbf{B}_S$ shows Cotton effects of the opposite sign at the same wavelengths. These isomeric compounds $\mathbf{B}_R$ and $\mathbf{B}_S$ when dipped into molar aqueous solution of azide turns into dark green coloured compound $\mathbf{C}_R$ and $\mathbf{C}_S$ respectively.

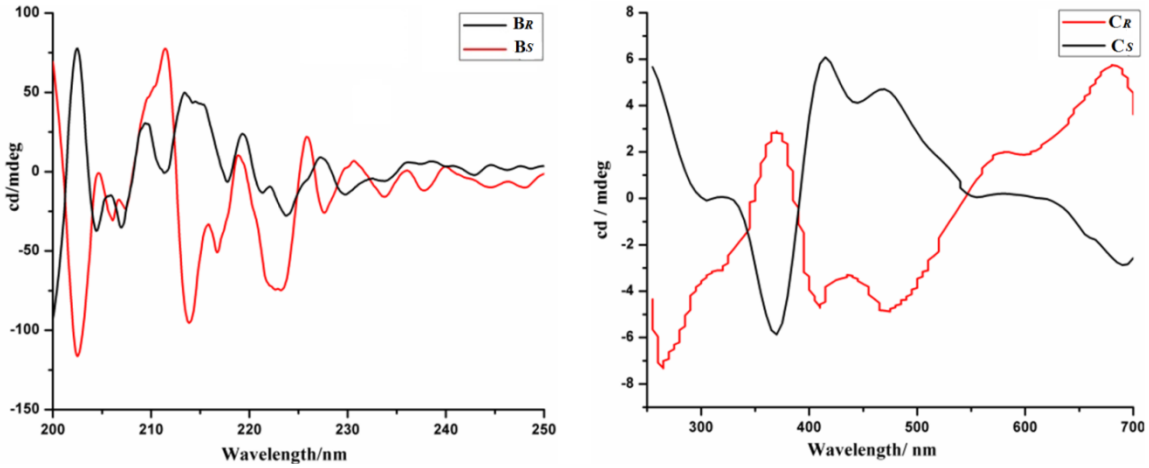

(a) (b)

Fig. 4.40: Solid state CD spectra in nujol (a) B_R and B_S; (b) C_R and C_S.

Compound $\mathbf{C}_R$ (*R*-isomer) showed positive Cotton effect around 365 nm and a negative cotton effect around 405nm and 460 nm after transformation from compound $\mathbf{B}_R$, while $\mathbf{C}_S$ (*S*-isomer) shows Cotton effects of the opposite sign at the same wavelengths from compound $\mathbf{B}_S$. CD spectroscopy confirms no change in sign of cotton effect during conversion of $\mathbf{B}_R$ to $\mathbf{C}_R$ i.e. *R*-isomer making it stereochemically unaltered bond breaking and bond formation. Hence it is important that chiral information has been fully transferred in this transformation.

Compound $\mathbf{C}_R$ and $\mathbf{C}_S$ when exposed to HCl vapours changes to yellowish green coloured also monitored by CD spectroscopy. CD spectroscopy confirms no change in sign of cotton effect during conversion of $\mathbf{C}_R$ to $\mathbf{B}_R$ and $\mathbf{C}_S$ to $\mathbf{B}_S$ making it stereochemically unaltered bond breaking and bond formation.

4.8 References

[1] S. Kitagawa, R. Kitaura, Noro Shin-ichiro; *Angew. Chem. Int. Ed.***2004**, *43*, 2334-2375.

[2] J.-M. Lehn, *Concepts and Perspectives*VCH, Weinheim **1995**.

[3] C. J. Adams, H. M. Colquhoun, P. C. Crawford, M. Lusi, A. G.Orpen; *Angew. Chem. Int. Ed.***2007**,*46*, 1124-1128.

[4] E. Coronado, M. Giménez-Marqués, G. M. Espallargas, L. Brammer; *Nat. Commun.* **2012**, *3*, 828.

[5] (a) A. K. Vishwakarma, P.S.Ghalsasi; *J. Therm. Anal. Calorim.* **2012**,*107*, 155-158; b)A. K. Vishwakarma, P. S. Ghalsasi, A. Navamoney, Y. Lan, A. Powell; *Polyhedron***2011**, *30*, 1565-1570.

[6] G. Zi, L. Xiang, Y. Zhang, Q. Wang, Z. Zhang; *Appl. Organomet. Chem.* **2007**, *21*, 177-182.

[7] L. Sabine, J. Becker, W. Christian, A. Miska, C. Kleeberg, U. Behrens, O. Walter, S. Schindler Chem. Eur. J. 2013, 19, 5342-5351.

[8] A. K. Vishwakarma Studies on multifunctional organic-inorganic hybrid compounds, **2013**.

[9] G. Mínguez Espallargas, M. Hippler, A. J. Florence, P. Fernandes, J. van de Streek, M. Brunelli, W. I. David, K. Shankland, L. Brammer; *J. Am. Chem. Soc.* **2007**, *129*, 15606-15614.

[10] $\mathbf{A_1}$ is not soluble in water therefore role of water in micro-crystallization is ruled out.

[11] The rate of reaction can be controlled by the concentrations of reactants and the flow of HCl gas.

[12] L. Mei, S. Jie, Z. Shi-Ming, Y. Hao, H. Ke-Liang, *Res. Chem. Intermed.* **2010**, *36*, 1049-1054.

[13] (a) H.-L. Zhu, P. Huang, C.-Y. Duan, L.-M. Zheng, Y.-J. Liu, M.-F. Wu, W.-X. Tang, *Transition Met. Chem.* **1999**, *24*, 380-383; (b) B. J. Hathaway, A. A. G. Tomlinson, *Coord. Chem. Rev.* **1970**, *5*, 1-43; (c) B. J. Hathaway, *J. Chem. Soc., Dalton Trans.* **1972**, 1196-1199.

[14] P. Chaudhuri, K. Oder, *J. Chem. Soc., Dalton Trans.* **1990**, 1597-1605.

[15] A. O. Polyakov, A. H. Arkenbout, J. Baas, G. R. Blake, A. Meetsma, A. Caretta, P. H. van Loosdrecht, T. T. Palstra; *Chem. Mater.* **2011**, *24*, 133-139.

[16] A. Caretta, R. Miranti, R. W. Havenith, E. Rampi, M. C. Donker, G. R. Blake, M. Montagnese, A. O. Polyakov, R. Broer, T. T. Palstra; *Phys Rev B* **2014**, *89*, 024301.

[17] E. Pardo, C. Train, H. Liu, L. M. Chamoreau, B. Dkhil, K. Boubekeur, F. Lloret, K. Nakatani, H. Tokoro, S. i. Ohkoshi; *Ang. Chem.* **2012**, *124*, 8481-8485.

[18] C. Zanchini, R. D. Willett, *Inorg. Chem.* **1990**, *29*, 3027-3030.

[19] S. Supriya, S. K. Das; *Chem. Commun.* **2011**, *47*, 2062-2064.

[20] Z.-G. Gu, Y. Song, J.-L. Zuo, X.-Z. You; *Inorg. Chem.* **2007**, *46*, 9522-9524.

[21] J. March, Advanced organic chemistry: reactions, mechanisms, and structure, Vol. 4, McGraw-Hill New York, **1968**.

[22] H. M. Mande, P. S. Ghalsasi, N. Arulsamy; *Cryst. Growth Des.* **2014**, *14*, 4254-4257.